

A Stratification in Magnetic Field Structures: The Radio Outflow in NGC 4151

SALMOLI GHOSH ,¹ PREETI KHARB ,¹ ELISA COSTANTINI ,^{2,3} JACK F. GALLIMORE ,⁴ DAVID WILLIAMS-BALDWIN ,⁵ AND MISSAGH MEHDIPOUR ,⁶

¹*National Centre for Radio Astrophysics (NCRA) - Tata Institute of Fundamental Research (TIFR), S. P. Pune University Campus, Ganeshkhind, Pune 411007, Maharashtra, India*

²*SRON Space Research Organisation Netherlands, Niels Bohrweg 4, 2333CA, Leiden, The Netherlands*

³*Anton Pannekoek Institute for Astronomy, Postbus 94249, 1090 GE Amsterdam, The Netherlands*

⁴*Department of Physics and Astronomy, Bucknell University, Lewisburg, PA 17837, USA*

⁵*Jodrell Bank Centre for Astrophysics, School of Physics and Astronomy, The University of Manchester Alan Turing Building, Oxford Road, Manchester M13 9PY Lancashire, United Kingdom*

⁶*Department of Astronomy, University of Michigan, 1085 South University Avenue, Ann Arbor, MI, 48109, USA*

ABSTRACT

The nature of radio outflows in radio-quiet AGN remains poorly understood. In this study, we present kpc-scale polarization observations of the Seyfert galaxy NGC 4151 using the Karl G. Jansky Very Large Array (VLA) in B-array at 3 and 10 GHz. We find that the inferred magnetic (B-) field structures show a stratification: a ‘spine-sheath’-like structure, with fields perpendicular to the jet direction in the ‘spine’ and parallel in the ‘sheath’, is observed in the higher resolution (0.5 arcsec) image at 10 GHz. In addition, a ‘wind’-like component with B-fields perpendicular to the radio outflow is observed in the 3 GHz image (resolution 2 arcsec); this feature is prominent along the ‘receding’ (eastern) jet direction. Rotation measure (RM) ranges from -230 to 250 rad m $^{-2}$ over the polarized regions, indicating a low-electron-density (10^{-2} – 10^{-3} cm $^{-3}$) tenuous medium surrounding the source causing Faraday rotation. A tentative RM gradient of $+75$ to -25 rad m $^{-2}$ is observed transverse to the northern ‘wind’ component, while a similar gradient with opposite sign is seen across the southern ‘wind’ component, suggestive of a helical magnetic field threading the outflow. Based on an analysis of the available radio and X-ray data, we conclude that the stratified radio outflow in NGC 4151 is magnetically-driven. The bi-conical radio ‘wind’ is found to be massive (1050 – 3200 M_{\odot}) with a high mass outflow rate (0.01 – 0.03 M_{\odot} yr $^{-1}$) but low in kinetic power (< 0.01% of L_{bol}), making it less impactful for galactic-scale feedback. Our study suggests that radio-quiet AGN may also host magnetically dominant jets and winds, even while their jets are smaller and weaker compared to radio-loud AGN.

Keywords: Seyfert Galaxies (1447) — Radio interferometry (1346) — Magnetic fields (994)

1. INTRODUCTION

While radio-quiet (RQ) Seyfert galaxies constitute the majority of nearby active galactic nuclei (AGN), the nature of their radio emission remains poorly understood (W. Ishibashi & T. J. L. Courvoisier 2011; F. Panessa et al. 2019; J. F. Radcliffe et al. 2021). Unlike their radio-loud (RL) counterparts ($R = S_{5 \text{ GHz}}/S_{B\text{-band}} > 10$; K. I. Kellermann et al. 1989), Seyfert galaxies typically host small and relatively weak radio jets that remain confined to their host galaxies. The origin of their radio emission on kpc scales has been suggested to be either AGN-jet or wind-related (E. J. M. Colbert et al. 1996a; B. Sebastian et al. 2020) or starburst-wind-related (S. A. Baum et al. 1993; G. Cecil et al. 2001) or a combination of both (S. Veilleux et al. 2005; S. Silpa et al. 2021). Very long baseline interferometry (VLBI) observations of Seyfert galaxies support the AGN-jet scenario in several Seyfert galaxies (M. Giroletti & F. Panessa 2009; P. Kharb et al. 2021), highlighting the greater complexity of radio outflows in RQ AGN compared to RL AGN.

NGC 4151 is a well-studied nearby ($z = 0.0033$) Seyfert type 1.5 galaxy (D. R. A. Williams et al. 2017). This barred spiral galaxy has also recently been identified as a changing-look AGN (CLAGN; H.-C. Feng et al. 2024). A wedge-shaped torus, a stratified broad-line region (BLR), an ultra-fast outflow from near the supermassive black hole (SMBH; $M_{\text{BH}} = 1.66^{+0.48}_{-0.34} \times 10^7 M_{\odot}$ in NGC 4151; M. C. Bentz et al. 2022), and a powerful accretion-disk-driven wind have been suggested to be present in this galaxy (F. Tombesi et al. 2011; V. E. Gianolli et al. 2023; X. Xiang et al. 2025). Mildly relativistic gas outflows ($v \sim 0.03c - 0.2c$) are suggested to be interacting with the ambient media and producing strong shocks, which are accelerating particles to high energies. This has been suggested to cause X-ray absorption in NGC 4151 as well as the emission of gamma rays and neutrinos (D. M. Crenshaw & S. B. Kraemer 2007; F. Tombesi et al. 2011; E. Peretti et al. 2025). It is interesting to note that the ‘radio-quiet’ NGC 4151 exhibits properties similar to radio-loud sources that possess highly relativistic jets.

NGC 4151 has a relatively low star formation rate (SFR) of $0.25 - 0.95 M_{\odot} \text{ yr}^{-1}$ (E. Peretti et al. 2025). There are suggestions of an over-density of gas in the bar fueling the AGN, and ‘AGN feedback’ quenching the star formation (A. Pedlar et al. 1992; C. G. Mundell et al. 1999). NGC 4151 shows a multi-layered jet structure at radio frequencies extending over 10 arcsec (~ 900 pc) at wavelengths of $6 - 20$ cm, and aligned with the polarized optical continuum emission (K. J. Johnston et al. 1982). Higher resolution images at 1.7 GHz show an elongated structure of size $3.5 \text{ arcsec} \times 0.5 \text{ arcsec}$, with a double source at the centre separated by 0.45 arcsec (R. V. Booler et al. 1982; P. Carra et al. 1990). The images by J. S. Ulvestad et al. (2005) reveal knotty jet components aligned in east-west direction at a position angle (PA) of $\sim 77^{\circ}$.

A 1.4 GHz study of NGC 4151 by C. G. Mundell et al. (1995, 2001) shows absorption against the eastern jet components, supporting the interpretation that the eastern jet is receding while the western jet is approaching us. Observations with the enhanced Multi Element Remotely Linked Interferometer Network (*e*-MERLIN) array reveal a factor of 2 increase in the radio peak flux density of the central-most component (first jet component) compared to what was observed 2 decades ago, indicating its variable nature. Furthermore, the flat spectral index core suggests that the jets are currently being powered by the AGN (D. R. A. Williams et al. 2017, 2020).

The emission-line region gas is extended with both aligned and non-aligned components with the radio outflow, suggesting the effects of both photoionization from the AGN and shock ionization by the jets (C. G. Mundell et al. 2003; J. Wang et al. 2011; D. R. A. Williams et al. 2017). Filamentary structures are observed in different emission lines as well, consistent with episodic activity and precession (e.g., D. R. A. Williams et al. 2017). The jet speed inferred from VLBI observations is low: an upper limit of $0.05c$ is inferred at a distance of 0.16 pc from the core (J. S. Ulvestad et al. 2005; D. R. A. Williams et al. 2017). The low jet speed has been suggested to arise from strong jet medium interaction (J. S. Ulvestad et al. 2005). X-ray observations of NGC 4151 have revealed quasi-periodically oscillating signals, most likely due to the accretion disk instabilities (Y. Yongkang et al. 2025). A long-term optical emission-line and continuum variability has also been studied for this galaxy, consistent with changes in accretion rate or an accelerating outflow from near the SMBH (e.g., A. I. Shapovalova et al. 2010).

In this paper, we present a radio polarimetric study of NGC 4151 at 3 and 10 GHz with the Karl G. Jansky Very Large array (VLA). We present rotation measure (RM), spectral index and depolarization images of the radio outflow. The paper consists of the following sections. Section 2 includes the observational details and the data reduction procedure. Section 3 presents our findings with Sections 3.1, 3.2, and 3.3 mentioning details about the radio structure and inferred B-fields, depolarization models, and properties of the observed ‘wind’ component. Section 4 discusses the implications of our findings. Section 5 presents the conclusions from this work. Throughout this paper, we adopt the λ cold dark matter cosmology with $H_0 = 67.8 \text{ km s}^{-1} \text{ Mpc}^{-1}$, $\Omega_{\text{mat}} = 0.308$, $\Omega_{\text{vac}} = 0.692$. Spectral index, α , is defined such that flux density at a frequency ν is $S_{\nu} \propto \nu^{\alpha}$.

2. OBSERVATIONS AND DATA ANALYSIS

We observed NGC 4151 with the VLA at 3 GHz (with a bandwidth of 2 GHz) and 10 GHz (with a bandwidth of 4 GHz) in B-array configuration on 2 August 2024 and 17 August 2024 (Project ID: 24A-122; PI: Salmoli Ghosh), yielding resolutions of ~ 2 arcsec (corresponding to ~ 0.2 kpc) and ~ 0.5 arcsec (corresponding to ~ 0.4 kpc), respectively. We used the **Common Astronomical Software Application** (CASA, version 6.6; THE CASA TEAM et al. 2022) to carry out the basic calibration for radio data, comprising initial data flagging, instrument-specific corrections, and solving for delays, bandpass, and complex gain terms. The solutions were refined with intermediate flagging until convergence was achieved. After applying the basic calibration, we attempted the polarization calibration on the data

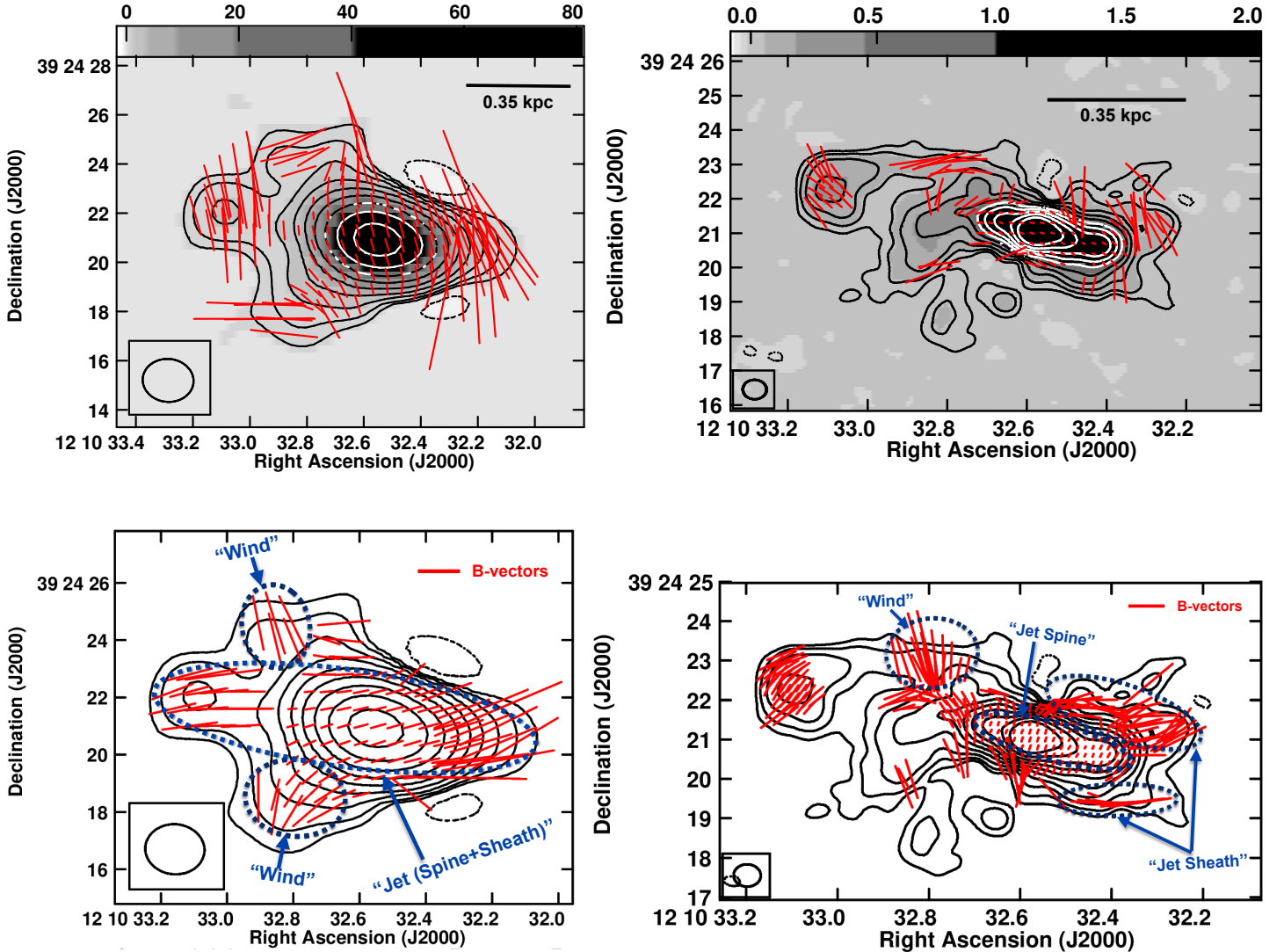


Figure 1. Top Left: 3 GHz image of NGC 4151 at a resolution of ~ 2 arcsec, obtained using the VLA B-array. The polarization vectors are shown in red ticks with 6 arcsec of length proportional to a fractional polarization of 10%. The contour levels shown in black are at 5σ ($\pm 1, 2, 4, 8, 16, 32, 64, 128, 256$) with $\sigma = 80 \mu\text{Jy beam}^{-1}$. The gray-scale varies from -0.8 to 80 mJy beam^{-1} in logarithmic scale. The dark horizontal line marks the distance scale of $\sim 350 \text{ pc}$ (4 arcsec). The synthesized beam shown at the bottom left corner of the image is of size $2.1 \text{ arcsec} \times 1.7 \text{ arcsec}$ at a PA of 85° . Top Right: 10 GHz image of NGC 4151 at a resolution of ~ 0.5 arcsec obtained using the VLA B-array. The polarization vectors are shown in red ticks with 2 arcsec proportional to a fractional polarization of 50%. The contour levels shown in black are at 3σ ($\pm 1, 2, 4, 8, 16, 32, 64, 128, 256, 512$) with $\sigma = 8 \mu\text{Jy beam}^{-1}$. The gray-scale varies from -0.07 to 2 mJy beam^{-1} in logarithmic scale. The synthesized beam is of size $0.7 \text{ arcsec} \times 0.6 \text{ arcsec}$ at a PA of 89° . Bottom Left & Right: Inferred magnetic-field vectors in the NGC 4151 outflow at 3 (left) and 10 GHz (right) by rotating EVPAs by 90° . The B-field shows a stratification and is found to be similar to what is predicted for a jet ‘spine’, jet ‘sheath’ and a magnetically driven ‘wind’ (e.g., R. A. Laing & A. H. Bridle 2014; M. Mehdipour & E. Costantini 2019). North is to the top and East to the left in this and all subsequent figures.

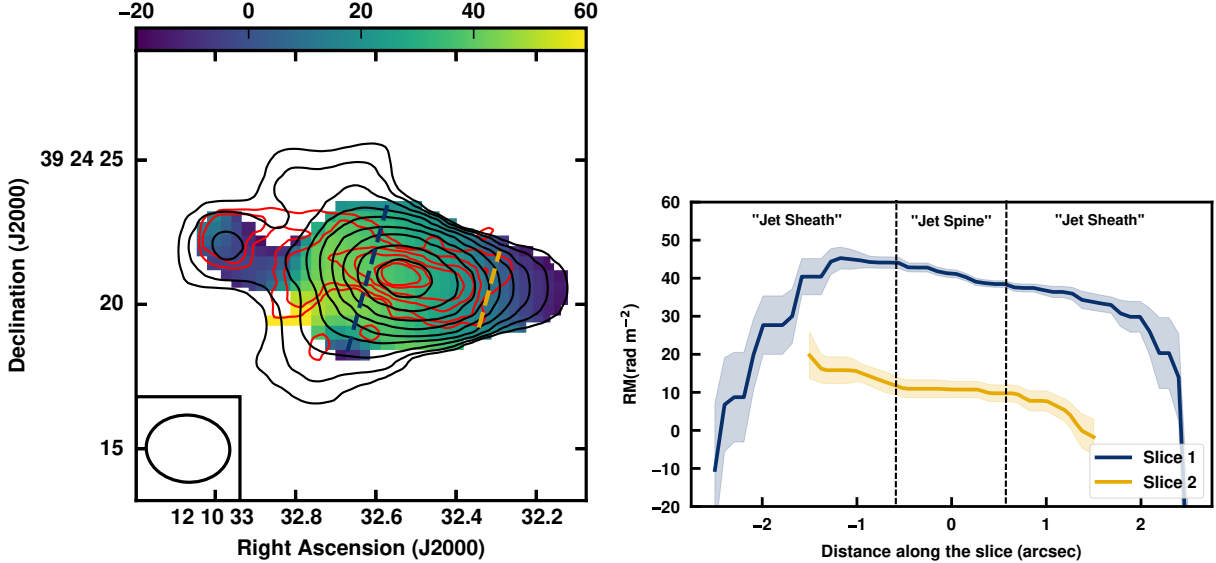


Figure 2. Left: The in-band 3 GHz RM image, blanked by an RM error of 20 rad m^{-2} . The 3 GHz contours are shown in black, the 10 GHz contours in red. The blue and the yellow dashed lines indicate the transverse slices taken across the jet. Right: The RM and RM error values are shown with a solid line and a shaded region, respectively, corresponding to the slices drawn on the left image. The slices taken from bottom to top on the left figure are represented from left to right on the right figure.

following the CASA-based VLA radio-polarimetric data reduction script⁷. The standard calibrator 3C286 with known polarization model was used to determine both leakage and the absolute polarization angle. The leakages were also derived using an unpolarized calibrator OQ208. Although both 3C286 and OQ208 produced similar values for leakages, solutions using OQ208 have been used, as they were better behaved and showed fewer outliers.

After applying the polarization calibration solutions, we imaged NGC 4151 using the TCLEAN task in CASA with the **Multi-term Multi-Frequency Synthesis** (MT-MFS; S. Bhatnagar et al. 2013) deconvolver, a **Robust** weighting of +0.5 and manual masking. We then carried out three rounds of phase-only self-calibration and two to three rounds of combined amplitude and phase self-calibration. The final output includes Stokes I, Q, U, and V images with a synthesized beam size of $2.1 \text{ arcsec} \times 1.7 \text{ arcsec}$ and $0.7 \text{ arcsec} \times 0.6 \text{ arcsec}$ and beam position angles of 85° and 89° with an r.m.s. noise of $80 \mu\text{Jy beam}^{-1}$ and $8 \mu\text{Jy beam}^{-1}$ at 3 and 10 GHz, respectively. The polarization quantities are estimated as: linear polarization fraction (f_p) = $\sqrt{Q^2 + U^2}/I$, and linear polarization angle (χ) = $0.5 \tan^{-1}(U/Q)$. The final polarization images have been made by plotting the electric vector position angles (EVPA) with the vector lengths proportional to f_p (see Figure 1; top panel). Figure 1 bottom panel presents the inferred B-field vectors with lengths proportional to f_p , obtained by rotating the EVPA by 90° . These images have been corrected for Galactic RM. The Galactic plus source RM corrected images are presented in Figure 8 in the Appendix and discussed ahead. We note that these images do not capture some of the diffuse polarized emission with higher RM uncertainties, in contrast to Figure 1.

We generated the in-band 3 GHz RM image by splitting the 3 GHz data into three sub-bands and running the task RMFIT in CASA to fit the resultant QU cubes. The in-band RM image has been blanked by RM error $> 20 \text{ rad m}^{-2}$ (see Figure 2, left panel). The right panel in Figure 2 shows the in-band 3 GHz RM values with the corresponding error values taken across the jet. The (Figure 3, top left panel) is generated by splitting the 10 GHz data into two sub-bands of 9 and 11 GHz, and the 3 GHz data. All images were made with the same image-size, cell-size, and beam. RMFIT is used to fit the three QU cubes made at the three frequencies for each pixel to obtain an RM image and an RM error image. The final RM image was made at a resolution of $2.1 \text{ arcsec} \times 1.7 \text{ arcsec}$ and a beam position angle of 89° , and blanked above an error value of $> 30 \text{ rad m}^{-2}$. It was also corrected for a Galactic RM value of $0.1 \pm 1.2 \text{ rad m}^{-2}$ (J. Xu & J.-L. Han 2014). The RM error image has been shown with error values from 0 to 40 rad m^{-2} in the top right

⁷ https://github.com/astrouser-salm/radio-imaging/blob/main/VLA_polarization_pipeline.py

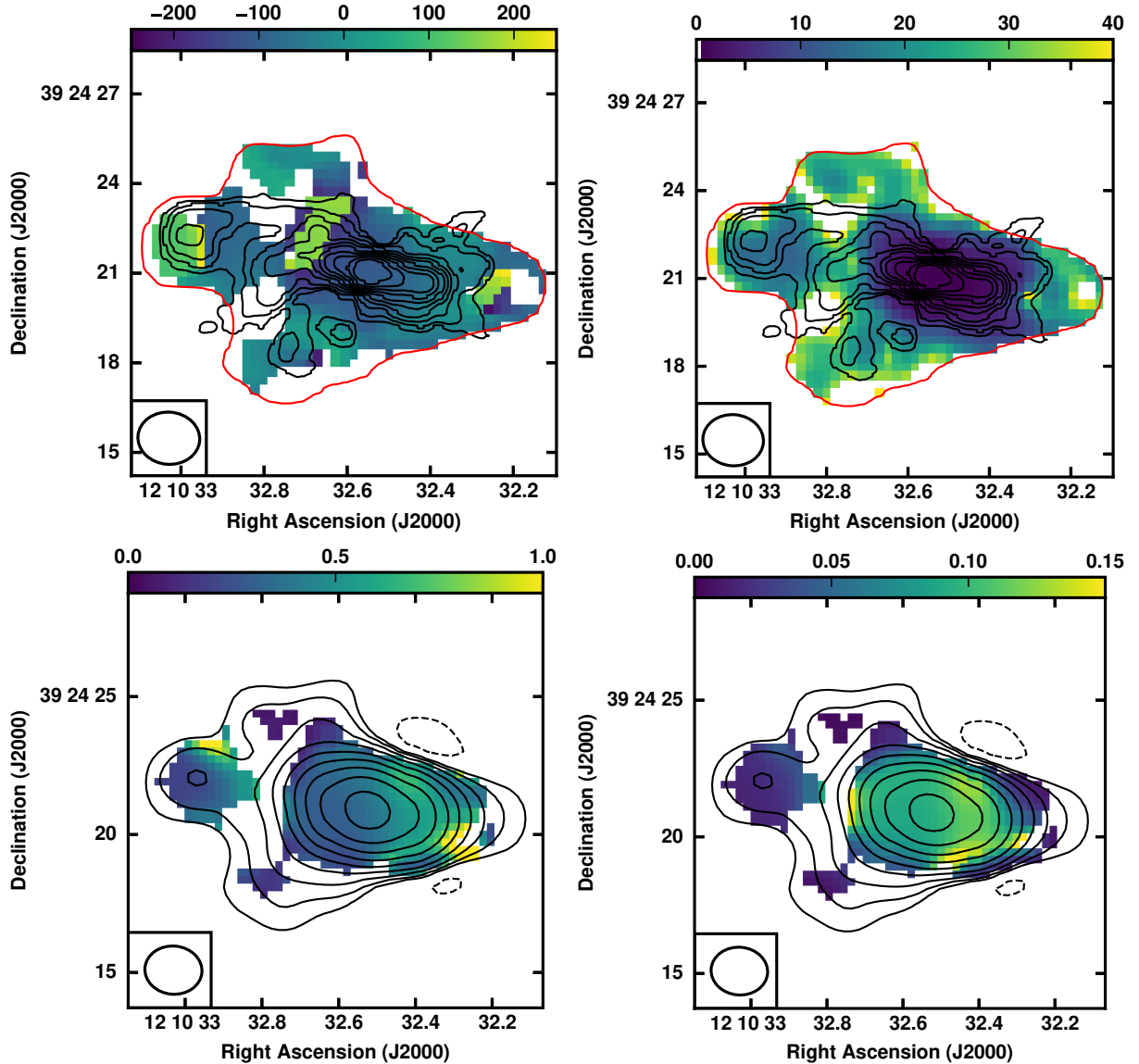


Figure 3. Top left: RM image of NGC 4151, using polarization data at 3 GHz, 9 GHz and 11 GHz, shown in color. The contours from 10 GHz data (Figure 1, right) are overplotted in black. The lowest contour from 3 GHz data has been shown in red. The RM values are shown from -200 to $+200$ rad m^{-2} . Top right: The RM error image shown in colour with values ranging from 0 to 40 rad m^{-2} . Bottom left: The depolarization image of NGC 4151 with values ranging from 0 to 1. The contours from 3 GHz data (Figure 1, left) are overplotted in black. Bottom right: The depolarization error image shown in colour with values ranging from 0 to 0.15.

panel of Figure 3. The depolarization image (Figure 3, bottom left panel) was obtained by dividing the fractional polarization image at the lower frequency (3 GHz) by that at the higher frequency (10 GHz). The depolarization image shows values extending from 0 to 1, with 1 indicating the lowest and 0 indicating the highest depolarization regions. The error on the estimated depolarization has been shown in the bottom right panel of Figure 3.

The RM image was constructed using only pixels with intensities above 3σ in each image, so the EVPAs and inferred B-field vectors in Figure 1 are shown without correction for the derived RM because most pixels are blanked when combining the RM, the f_p and the χ images. The 10 GHz EVPAs (and inferred B-field vectors) remain unchanged within their uncertainties (as expected at shorter wavelengths; see Equation 1). At 3 GHz, the EVPA orientations are broadly similar except in the core and hotspot regions, where RM values of ~ 100 rad m^{-2} cause $\sim 50^\circ$ rotations, aligning the core vectors to the vectors found in the 10 GHz jet ‘spine’. Source RM-corrected B-field images for

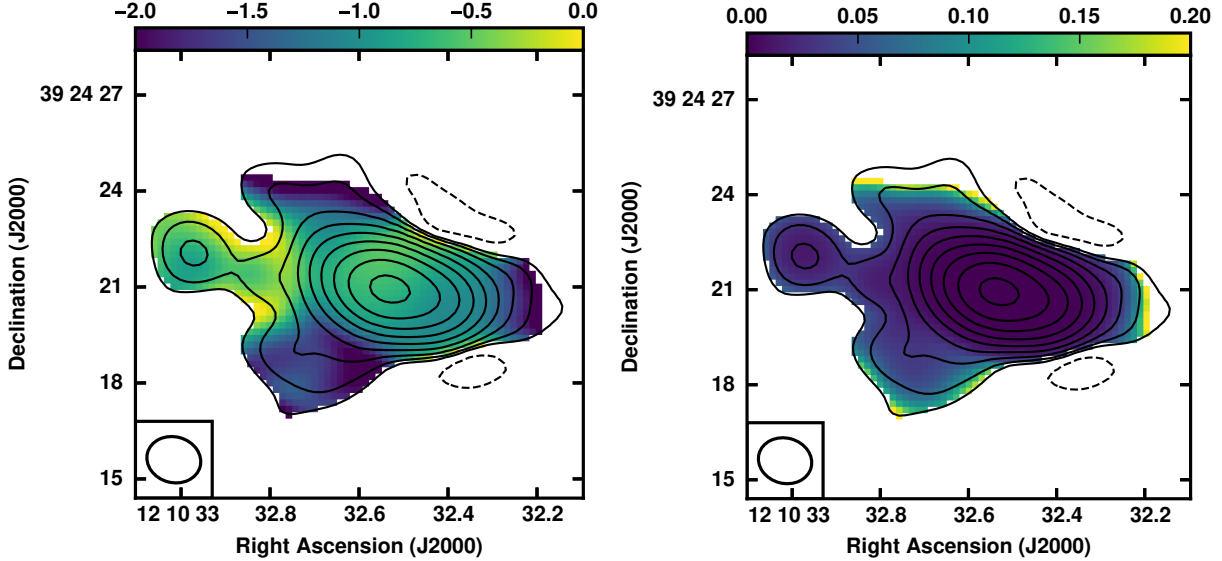


Figure 4. Left: Spectral index image made from 3 GHz and 10 GHz total intensity images. The spectral index values are shown in colour with values ranging from -2 to 0 . The uniformly weighted 3 GHz Stokes I image has been overlaid with black contours with levels similar to Figure 1, left panel. The synthesized beam is of size $1.7 \text{ arcsec} \times 1.4 \text{ arcsec}$ at a PA of 75° . Right: The spectral index error image in colour with values ranging from 0 to 0.2 .

both 3 and 10 GHz, as shown in Figure 8 in the Appendix, have been created by plotting the EVPA vectors with magnitude f_p at individual frequencies and with angles from the pa0 (polarization angle at 0 wavelength, i.e., source RM-corrected) image produced by the `rmfit` task in `CASA` blanked by its respective error image (with errors $> 10\%$), and finally rotated by 90° to obtain the B-vectors.

The two-frequency spectral index image has been created using the 3 GHz and 10 GHz total intensity images made with the same `uvrange` and `uvtaper` in terms of wavelength, and a robust parameter of -1.5 (for 3 GHz) and $+1.5$ (for 10 GHz). Finally convolving them using an identical restoring beam in `tclean`, the spectral index image was created at a synthesized beam size of $1.7 \text{ arcsec} \times 1.4 \text{ arcsec}$, at a PA of 75° . The spectral index image was then blanked by the spectral index noise image with spectral index errors > 0.3 , which has been further blanked by a total intensity value less than 3σ , to obtain the final image (Figure 4, left panel). The corresponding error image is shown in the right panel of Figure 4.

3. RESULTS

A multi-component radio outflow is revealed in our VLA observations. The inferred magnetic field structures imply the presence of three distinct components, which we suggest to be a jet ‘spine’, jet ‘sheath’, and a possible ‘wind’ component. Using ‘minimum energy’ estimates and RM, we derive constraints on the depolarizing medium in NGC 4151.

3.1. Radio Morphology & B-field Structures

The lower-resolution VLA image at 3 GHz reveals two primary components: a jet ($\text{PA} \approx 80^\circ$) and a transverse extension on both sides of the jet, which we identify to be the ‘wind’. The jet shows an inferred B-field that is almost aligned with the outflow direction, with a fractional polarization of $f_p \approx 0.9\%$. In contrast, the ‘wind’ component ($\text{PA} \approx 90^\circ$) exhibits higher polarization ($f_p \approx 3\%$) with EVPAs $\chi = \pm 70^\circ$, negative on the northern side and positive on the southern side. This implies a B-field orientation of $\approx \pm 20^\circ$, respectively, which is roughly perpendicular to the outflow. The 10 GHz image further resolves the jet into two components: an inner ‘spine’ with inferred B-fields perpendicular to the outflow and an outer ‘sheath’ layer with inferred B-field aligned with the outflow. We observe a maximum lateral extent of $\sim 9 \text{ arcsec}$ ($\sim 0.8 \text{ kpc}$) on the east side of the core, and $\sim 4 \text{ arcsec}$ ($\sim 0.3 \text{ kpc}$) on the western side. The eastern outflow extends longer as well compared to the western side by about 2.5 arcsec ($\sim 0.2 \text{ kpc}$).

We note that the lower resolution 3 GHz image shows polarized structures that are consistent with those observed in the higher resolution 10 GHz image. The regions with the highest fractional polarization at 10 GHz dominate

the polarized emission in the 3 GHz image, as seen especially clearly in the regions at the jet extremities. In the other regions, a vector averaged B-field structure is observed (over and above the global Faraday rotation). This is consistent with the 10 GHz image re-created using the 3 GHz synthesized beam. Moreover, the in-band RM image centered around 3 GHz (see Section 3.2) shows the signatures of two regions with different RM values, consistent with the spine-sheath structure observed at 10 GHz, as discussed in greater detail ahead.

The jet ‘spine’ on the western side is brighter than the eastern one, suggesting that the western jet is the approaching one and is mildly Doppler-boosted as suggested by the VLBI observations of D. R. A. Williams et al. (2017). We have estimated the jet-to-counterjet brightness ratio (R_J) by comparing the flux densities of the western versus eastern jet-spine. Considering an inclination angle (θ) of 40° (M. Ruiz et al. 2003), the velocity (βc) obtained using $\beta = \frac{R_J^{1/(2-\alpha)} - 1}{\cos \theta (R_J^{1/(2-\alpha)} + 1)}$ (C. M. Urry & P. Padovani 1995) is $\sim 0.16c$ at 0.1 kpc from the nucleus. The ‘wind’ component can only be observed on the receding side of the jet. Similar structures have been observed in other astrophysical sources as well; for instance, in the protostar Hops 315 (C. Vleugels et al. 2025). R. A. Laing et al. (2006) note that if the jets are relativistic and faster on-axis rather than at their edges (i.e. a velocity stratification), then the approaching jet appears more centre-brightened than the receding one.

The observed two-frequency spectral index image reveals a core spectral index of $\alpha \approx -0.66$, and a jet spectral index of $\alpha \approx -0.8$, consistent with synchrotron emission in a collimated outflow. The shocked region on the eastern side appears to have flatter α of ≈ -0.64 , indicating a re-acceleration of charged particles in that region. By contrast, the southeastern wind-feature is markedly steeper with $\alpha \approx -1.55$, suggesting a rapidly ageing electron population undergoing significant radiative, inverse Compton, and adiabatic losses as it expands. The jet kinetic power, estimated from the core flux density at 5 GHz (extrapolated from 45.5 mJy at 10 GHz assuming $\alpha = -0.66$ at the core) using the empirical relation of A. Merloni & S. Heinz (2007), is found to be $\sim 10^{43}$ erg s $^{-1}$. This places NGC 4151 toward the upper end of kinetic powers observed in typical radio-quiet AGN (e.g., P. Kharb et al. 2021). The depolarization image (Figure 3, right panel) indicates that the winds are predominantly depolarized. The receding jet is more depolarized compared to the approaching one, likely due to the Laing-Garrington effect (R. A. Laing 1988; S. T. Garrington et al. 1988); that is, due to the presence of excess depolarizing material (see C. G. Mundell et al. 1995, which describes the presence of an HI disk) towards the receding jet.

3.2. Deriving Constraints on the Depolarizing Media from RM

When polarized light traverses a magneto-ionized medium, it undergoes Faraday rotation (e.g., R. Beck & R. Wielebinski 2013). The difference between the observed angle of polarization (χ_{obs}) and the intrinsic angle of polarization (χ_{int}) is given by

$$\chi_{obs} - \chi_{int} = \text{RM} \times \lambda^2 \quad (1)$$

where λ is the wavelength. RM is dependent on the electron density (n_e), line of sight B-field (B_{\parallel}) and the length of the Faraday rotating medium (L) as

$$\text{RM (rad m}^{-2}\text{)} = 812 n_e (\text{cm}^{-3}) B_{\parallel} (\mu\text{G}) L (\text{kpc}) \quad (2)$$

We created an in-band RM image using the 3 GHz polarization data as well as a broadband RM image using both the 3 GHz and 10 GHz polarization data. The in-band RM image is affected by differential Faraday rotation within the 3 GHz emitting regions (see Figure 2), even though these ‘layers’ are not distinctly resolved in the 3 GHz polarization image (Figure 1, left panel). We find that RM values are higher in the inner jet region and show a decrease towards the edges. We note that the RM uncertainty as reported by the CASA task `rmfit`, and plotted in Figure 2, corresponds to the 1σ error from a weighted linear fit of polarization angle versus wavelength squared, with weights derived from the Q and U noise. While the wider transverse slice (Slice 1 in Figure 2) shows an RM difference in the spine-sheath region at or greater than the $\sim 2\sigma$ level, the RM values become similar in the spine-sheath region in the narrower slice (Slice 2 in Figure 2) at the $\sim 2\sigma$ level. While marginal, the in-band RM structure supports the picture of jet stratification. The lower RM values in the ‘sheath’ may indicate a reduction in either the magnetic field strength, the electron density, or the effective path length of the Faraday-rotating medium. The enhanced depolarization observed in the ‘sheath’ compared to the ‘spine’ (see Figure 3, bottom left panel) may arise from gas entrainment and ‘mass loading’, leading to enhanced electron density. Assuming comparable path lengths for the Faraday-rotating medium in both the jet ‘spine’ and ‘sheath’, the observed decrease in RM going from the ‘spine’ to the ‘sheath’ could also point to greater magnetic field strength along the jet axis and lesser towards the edges (e.g., R. A. Laing 1980; R. A. Laing

Table 1. Observed radio properties of NGC 4151

Region	3 GHz					10 GHz				
	S_{tot} (mJy)	f_p (%)	χ ($^{\circ}$)	α	RM (rad m $^{-2}$)	S_{tot} (mJy)	f_p (%)	χ ($^{\circ}$)	α	RM (rad m $^{-2}$)
Total	221 \pm 11	3.25 \pm 0.6	88 \pm 4	12 \pm 3
Core	148 \pm 25	0.87 \pm 0.02	16 \pm 5	-0.66 \pm 0.03	-104 \pm 2	45.5 \pm 1	2.2 \pm 0.03	73 \pm 1	-0.63 \pm 0.03	-104 \pm 2
Eastern Hotspot	1.7 \pm 0.3	2.8 \pm 0.6	10 \pm 6	-0.64 \pm 0.02	70 \pm 20	0.18 \pm 0.01	12.5 \pm 2	50 \pm 2	-0.62 \pm 0.04	50 \pm 30
Western Jet-edge	1.0 \pm 0.2	6 \pm 1	31 \pm 6	-1.9 \pm 0.1	...	0.10 \pm 0.01	28 \pm 8	20 \pm 4	-1.1 \pm 0.1	-24 \pm 10
Western Jet	25 \pm 8	1.2 \pm 0.1	14 \pm 1	-0.9 \pm 0.1	-40 \pm 4	4 \pm 1	1.8 \pm 0.4	60 \pm 2	-0.95 \pm 0.03	70 \pm 10
Eastern Jet	25 \pm 2	0.7 \pm 0.2	17 \pm 2	-0.70 \pm 0.02	-60 \pm 25	3 \pm 1	2.9 \pm 0.5	66 \pm 3	-0.66 \pm 0.04	-131 \pm 5
Southern Wind	0.9 \pm 0.2	2.4 \pm 0.6	63 \pm 8	-1.55 \pm 0.05	-28 \pm 8	0.12 \pm 0.01	-1.5 \pm 0.4	-29 \pm 3
Northern Wind	0.6 \pm 0.2	3.3 \pm 0.3	-70 \pm 8	-2.2 \pm 0.2	28 \pm 7	0.18 \pm 0.05	33 \pm 1	-68 \pm 4	-0.8 \pm 0.2	...

Note: Column 1: Region of interest. The regions are chosen as square boxes of width \sim 1.5 arcsec and \sim 1 arcsec for 3 and 10 GHz images, respectively and are defined as follows. ‘Core’ is unresolved base of the jet in Figure 1. ‘Eastern Hotspot’ is the region of shocked emission \sim 6.3 arcsec away from the core. ‘Western Jet-edge’ is the region of high polarization fraction (the jet ‘sheath’ observed at 10 GHz) \sim 4.6 arcsec to the west of the core at 3 GHz (\sim 3.5 arcsec west of the core at 10 GHz). ‘Western Jet’ is the western part of the jet as shown in Figure 1, left panel, \sim 2.2 arcsec from the core towards the west. The ‘Eastern Jet’ denotes the region \sim 2 arcsec to the east of the core. The ‘Western Jet’ and ‘Eastern Jet’ at 10 GHz are the regions along the jet ‘spine’ as shown in Figure 1, right panel, at \sim 1.7 and \sim 1.3 arcsec from the core in the 10 GHz image. The ‘Southern Wind’ and the ‘Northern Wind’ at 3 GHz include the ‘wind’ regions shown in Figure 1 \sim 3 and \sim 4 arcsec to the south and the north of the core, respectively. The ‘Northern Wind’ and ‘Southern Wind’ at 10 GHz denote regions about \sim 2 arcsec north, \sim 2.5 arcsec east and \sim 2.6 arcsec south, \sim 2.7 arcsec east of the core, respectively. Column 2: Total flux density of the chosen region in mJy. For compact features such as the ‘core’ and the ‘Eastern Hotspot’, the peak intensity has been noted. Column 3: Mean fractional polarization in the region of interest. Column 4: Mean polarization angle in the considered region, only if the vectors are aligned in a similar direction. No data implies that vectors are oriented in multiple directions within that region, or polarization is not detected. Column 5: The mean 3 GHz – 10 GHz spectral index in the region. Column 6: The mean rotation measure estimate in the region of choice. No data indicates that the RM has a rapid change in values and a high error ($>60\%$ of the absolute value) due to the low SNR of polarized emission in one of the three frequencies, or is undetected. Column 7 – 11: Same as in Column 1 – 6, estimated from the 10 GHz data. The α values here are the mean 3 GHz – 10 GHz spectral index values for the regions of choice.

& A. H. Bridle 2002). A combination of ‘magnetic flux’ and ‘mass loading’ have indeed been suggested to influence the creation of collimated outflows in protostellar as well as AGN jets in simulations (e.g., C. Fendt 2006; R. E. Pudritz et al. 2006).

The RM in NGC 4151 is found to change its value and sign rapidly in the kpc-scale region, with values ranging from -230 to 250 rad m $^{-2}$. A transverse RM gradient is observed across the ‘wind’ components (see Section 3.3). Since each ‘wind’ region is comparable to the size of the synthesized beam, the RM is likely to be influenced by systematic uncertainties. However, the northern and southern ‘wind’ regions display RM of comparable magnitude but opposite signs. Taken together, their combined RM structure would be consistent with a transverse gradient assuming that these regions belonged to a single physical component (e.g., a wide-angled bi-conical wind). RM gradients transverse to parsec-scale jets have been observed in several RL AGN (K. Asada et al. 2002; T. Hovatta et al. 2012), on the \sim 100 parsec scale jet in M87 (A. Pasetto et al. 2021), as well as some RQ AGN (S. Ghosh et al. 2025a). These gradients have been suggested to arise due to the presence of helical B-fields (S. P. O’Sullivan & D. C. Gabuzda 2009; D. C. Gabuzda et al. 2004; P. Kharb et al. 2009). The mean RM observed at the 0.5 arcsec and 2 arcsec cores are -109.5 ± 0.5 and -103.1 ± 0.7 rad m $^{-2}$.

We have estimated the magnetic field strength (B_{min}), total energy (E_{total}) and the electron lifetimes (τ) in the core of NGC 4151, at two different resolutions, assuming the ‘minimum energy’ condition and using the relations from H. van der Laan & G. C. Perola (1969); A. G. Pacholczyk & J. S. Scott (1976); C. P. O’Dea & F. N. Owen (1987). At the core, the volume-filling factor (ϕ) of the radio plasma is assumed to be 1. The proton-to-electron energy ratio (k) is varied from 1 to 100 (e.g., T. N. La Rosa et al. 2006; D. R. A. Williams et al. 2017; S. Ghosh et al. 2025a). The core peak flux density was estimated by fitting a Gaussian component to the central region of width equal to the FWHM of the synthesized beam. The α values are obtained as the average spectral index in the core region. The

‘minimum energy’ B-field strength for the 0.5 arcsec and 2 arcsec cores at 10 and 3 GHz was estimated as $100 - 300 \mu\text{G}$ and $50 - 150 \mu\text{G}$ for $k = 1 - 100$, respectively. Similarly, the total energies are found to be $(3 - 30) \times 10^{52} \text{ erg}$ and $(20 - 200) \times 10^{52} \text{ erg}$ for $k = 1 - 100$, in the cases of 0.5 arcsec and 2 arcsec cores, respectively. The electron lifetimes for synchrotron and CMB losses are obtained as $(2.5 - 0.5) \times 10^5 \text{ yrs}$ and $(1.5 - 0.3) \times 10^6 \text{ yrs}$, respectively.

Assuming $B_{min} \equiv B_{\parallel}$ (see I. J. Feain et al. 2009; P. Kharb et al. 2009), and L to be the extent of the core, we estimate the electron densities to be in the range of $0.006 - 0.02 \text{ cm}^{-3}$ and $0.004 - 0.01 \text{ cm}^{-3}$, respectively. The inferred electron density of $10^{-2} - 10^{-3} \text{ cm}^{-3}$ for a Faraday rotating medium $0.06 - 0.2 \text{ kpc}$ in extent, with B-fields of strength $10^2 - 10^3 \mu\text{G}$, is low compared to typical n_e values observed in the warm ionized medium ($n_e \sim 0.1 \text{ cm}^{-3}$; J. M. Cordes & T. J. W. Lazio 2002; B. M. Gaensler et al. 2008). Such low electron densities suggest that the Faraday screen may consist of a tenuous, magnetized sheath or cocoon around the jet (e.g., R. A. Laing et al. 2008; M. M. Lisakov et al. 2021).

3.2.1. Media Characteristics for External and Internal Depolarization

The polarized emission from the sources is modified by the intervening medium through Faraday rotation, which alters the observed polarization angle and can also reduce the degree of polarization. When the Faraday-rotating medium lies between the source and the observer, the effect is referred to as external depolarization. Conversely, when the rotating medium is mixed with the source plasma itself, the effect is referred to as internal depolarization.

In the case of external depolarization, the fractional polarization (f_p) at a particular wavelength (λ) can be expressed following B. J. Burn (1966); W. van Breugel & E. B. Fomalont (1984) as

$$f_p(\lambda^2) = f_{pi} \exp\{-2(812 n_e B_{\parallel})^2 d R \lambda^4\} \quad (3)$$

For the 2 arcsec core, we considered an $n_e = 0.5 \times 10^{-2} \text{ cm}^{-3}$ (see Section 3.2), and for a length (R) of 0.2 kpc (length of the core), and the line of sight magnetic field (B_{\parallel}) of $100 - 300 \mu\text{G}$, and estimated a polarization fraction of $0.87\% \pm 0.02\%$ and $2.2\% \pm 0.03\%$ at 0.1 m and 0.03 m of wavelength (λ), respectively. This yields an intrinsic polarization fraction (f_{pi}) of 2.22% and a fluctuation scale (d) of $0.01 - 0.1 \text{ kpc}$.

In the case of internal depolarization, the mixing of the plasma introduces a randomized (but isotropic) component (B_{rand}) of the B-field apart from the uniform component (B_{uni}). The total B-field can be represented as $B_{\text{tot}}^2 = B_{\text{uni}}^2 + B_{\text{rand}}^2$. The complex fractional polarization at a particular wavelength can now be given as (see, B. J. Burn 1966; A. G. Pacholczyk 1970; S. P. O’Sullivan et al. 2013)

$$P(\lambda^2) = f_{pi} \frac{1 - e^{-S}}{S} \quad (4)$$

where

$$S = 2(812 n_e B_{\text{rand}})^2 d L \lambda^4 - 1624i n_e B_{\text{uni}} L \lambda^2 \quad (5)$$

and

$$f_{pi} = f'_{pi} (B_{\text{uni}}^2 / B_{\text{tot}}^2). \quad (6)$$

The theoretical polarization fraction for $B_{\text{rand}} = 0$ for synchrotron radiation in optically thin regions (f'_{pi}) is given as $\frac{3-3\alpha}{5-3\alpha}$. For an α of ≈ -0.66 for the core, we obtained $f'_{pi} = 70\% \pm 1\%$ and $B_{\text{rand}}/B_{\text{uni}} = 5.55 \pm 0.04$. Assuming, $B_{\text{uni}} = \sqrt{3}B_{\parallel}$ (see B. J. Burn 1966; S. P. O’Sullivan et al. 2013), and B_{\parallel} to be $100 - 300 \mu\text{G}$, we obtain B_{uni} to be $170 - 520 \mu\text{G}$ and B_{rand} to be $0.96 - 2.88 \text{ mG}$ and therefore B_{tot} to be $0.97 - 2.93 \text{ mG}$. We use Equation 5 to find the electron density, $n_e \approx 6 \times 10^{-3} \text{ cm}^{-3}$. If thermal gas is mixed with the synchrotron plasma and causes depolarization, the total mass of it in the ‘core’ region can be estimated as $M_{tg} \sim n_e \phi m_H V$, where the volume filling factor ϕ is assumed to be unity, total volume of the lobes $V \approx 4.4 \times 10^{62} \text{ cm}^3$ (assuming a cylindrical volume), and mass of ionised hydrogen is $m_H = 1.67 \times 10^{-24} \text{ g}$. We find that a thermal gas mass of $M_{tg} \approx (2.21 \pm 0.18) \times 10^3 \text{ M}_{\odot}$ could be mixed in the ‘core’ region causing ‘core’ depolarization.

3.3. ‘Wind’ Kinematics in NGC 4151

We now derive the kinetic power and mass outflow rate of the ‘wind’ in NGC 4151, assuming it to be like a hollow cone around the jet. When the jets interact with the surrounding media, they inflate overpressured cocoons of relativistic plasma as proposed for Cygnus A by M. C. Begelman & D. F. Cioffi (1989) and the hydrodynamical simulations of D. F. Cioffi & J. M. Blondin (1992). The cocoon then drives shocks into the ambient gas, accelerating the neutral

and ionized gas into high-speed outflows (up to thousands of km s^{-1}). Alternatively, cocoons have been suggested to originate from precessing jets, as observed in the Galactic microquasar, SS 433 (C. S. Kochanek & J. F. Hawley 1990; K. M. Blundell & M. G. Bowler 2005). Interestingly, jet precession has been invoked in NGC 4151 by J. S. Ulvestad et al. (1998). However, using the formalism of R. M. Hjellming & K. J. Johnston (1981), we find that the entire radio structure cannot be fitted by a single continuously precessing jet. Rather, at least two separate episodes of jet precession are required to fully model the inner jet and the outer S-shaped lobes. We therefore suggest that the wide-angled ‘wind’ component is anchored to the accretion disk, similar to the radio jet. A conical morphology can naturally arise from initially weakly collimated outflows, shaped by the outward magnetic pressure of the accelerating plasma and/or by radial gradients in the magnetic field strength anchored in the accretion disk. Such conditions can give rise to hollow, conical winds with half-opening angles of $\sim 30\text{--}40^\circ$ (e.g., M. M. Romanova et al. 2009).

The kinetic energy, momentum and the mass outflow rate are given by

$$E_{\text{kin}} = \frac{1}{2} M_{\text{out}} v_{\text{out}}^2 \quad (7)$$

$$p_{\text{out}} = M_{\text{out}} \cdot v_{\text{out}} \quad (8)$$

$$\dot{M}_{\text{out}} = \frac{M_{\text{out}} v_{\text{out}}}{R_{\text{out}}} \quad (9)$$

Some of the gas may be entrained within the turbulent boundary layer of the jet, accelerating to significant speeds without being fully ionized. The thermal pressure inside the cocoon can also push it outward to form the outflow, which is effective within radii of 1 to 10 kpc, where cooling and mixing can occur. Comparing the flux densities of the inferred jet (‘spine+sheath’; $\approx 90 \text{ mJy}$) and the ‘wind’ component ($\approx 9.9 \text{ mJy}$), the ‘wind’ power is found to be 10 – 12% of that of the jet. In the ‘wind’ region $\sim 400 \text{ pc}$ from the centre, the absolute value of $|\text{RM}|$ is found to be around 28 rad m^{-2} . Assuming the ‘minimum energy’ condition and $k = 1 - 100$, $\phi = 0.5$ (A. J. Blustin & A. C. Fabian 2009) for a clumpy wind medium, and a hollow cone of outer, inner radius and a height of $\sim 400 \text{ pc}$, $\sim 130 \text{ pc}$, and $\sim 280 \text{ pc}$, respectively, the B-field in the wind region is found to be $27 - 82 \mu\text{G}$ with $n_e \sim 0.002 - 0.006 \text{ cm}^{-3}$. From A. J. Blustin & A. C. Fabian (2009); C.-A. Faucher-Giguère & E. Quataert (2012), $M_{\text{wind}} \approx n_p f m_p V$, where f is the filling factor. We assume f to be 0.5 for homogeneous emission and $n_p \approx n_e$. Therefore, the mass of the ‘wind’ component is found to be $1050 - 3200 M_{\odot}$. Assuming the velocity of the ‘wind’ to be 10% of that of the jet, i.e., $0.008c$ (also see F. Fiore et al. 2017; M. Perucho et al. 2017), we estimate the wind mass outflow rate to be $0.01 - 0.03 M_{\odot} \text{ yr}^{-1}$, and the wind kinetic energy to be $(12 - 36) \times 10^{52} \text{ erg}$. The spread in the derived estimates emerges from the range of k values adopted in the calculations.

A jet-driven secondary shock outflow, as may be present in NGC 4151, has also been suggested for other Seyfert galaxies by D. May & J. E. Steiner (2017); P. F. Hopkins & M. Elvis (2010). The typical starburst-driven galactic wind outflows are found to be much more powerful, with mass outflow rates up to $10 M_{\odot} \text{ yr}^{-1}$ and velocities of $100 - 500 \text{ km s}^{-1}$ (D. K. Strickland & I. R. Stevens 2000; S. Veilleux et al. 2005). Seyfert galaxy winds are often highly ionized, with lower mass outflow rates of $\sim 0.1 - 1 M_{\odot} \text{ yr}^{-1}$ but higher velocities (up to thousands of km s^{-1}), and greater kinetic energy per unit mass (S. Veilleux et al. 2005). Therefore, for NGC 4151, the observed wind appears to be weak. The kinetic power associated with the outflow is given by $\dot{E}_{\text{kin}} = \frac{1}{2} \dot{M}_{\text{out}} v_{\text{out}}^2$, is $(3 - 10) \times 10^{40} \text{ erg s}^{-1}$.

Following N. L. Zakamska & J. E. Greene (2014), we independently estimated the kinetic power of an AGN-driven wind from the radio emission, adopting a conversion efficiency of 3.6×10^{-5} . We computed the radio luminosity of the wind region at 1.4 GHz as νL_{ν} , where $L_{\nu} = 4\pi D_L^2 S_{\nu} (1+z)^{-(\alpha+1)}$ with D_L , S_{ν} , z , and α being the luminosity distance, flux density at frequency ν , redshift, and spectral index, respectively. We adopted an α of -1.8 , corresponding to the mean value measured for the northern and southern wind components (Table 1), and extrapolated the 1.4 GHz flux density from the 3 GHz data by summing the flux densities of the two (north and south) wind regions (the wind flux density estimated at 3 GHz is $1.5 \pm 0.4 \text{ mJy}$). Using this approach, we obtained a monochromatic radio luminosity of L_{radio} of $\sim 2.2 \times 10^{36} \text{ erg s}^{-1}$, and a wind kinetic power (\dot{E}_{kin}) of $\sim 5.9 \pm 1.6 \times 10^{40} \text{ erg s}^{-1}$. The uncertainty here is propagated from the uncertainty in the flux density. This value is consistent with our independent estimate of the wind kinetic power derived above from the outflow mass and velocity within the derived uncertainties for both the estimates.

Hence, the coupling efficiency $\epsilon_f = \dot{E}_{\text{kin}}/L_{\text{bol}}$, using a bolometric luminosity of $10^{44} \text{ erg s}^{-1}$ (S. B. Kraemer et al. 2021), is found to be $10^{-4} - 0.005$. That is, the wind kinetic power is only 0.01 – 0.5% of L_{bol} . This coupling efficiency lies at the lower end of the 0.1–10% range derived for radiatively-driven AGN winds (F. Fiore et al. 2017;

(N. L. Zakamska & J. E. Greene 2014), supporting the possibility of ionised winds creating the radio-emitting cocoon. However, this is too small for galaxy-scale AGN feedback, which has typically been observed in systems with kinetic power that is at least 0.5% L_{bol} (e.g., A. Merloni & S. Heinz 2007). Rather, it is consistent with a modest AGN-driven magnetohydrodynamic (MHD) wind, which may influence the immediate ISM but not provide galaxy-wide feedback. We note that the properties of the radio ‘wind’ are consistent with the warm absorbers detected in X-rays as described in Section 4.3.

4. DISCUSSION

4.1. A stratification in the B-field structure

The inferred B-field vectors show sharp changes in orientation with respect to the jet direction. We identify three layers as a jet ‘spine’, a jet ‘sheath’, and a ‘wind’ component. The inferred B-field is perpendicular in the jet spine. This is consistent with a jet dominated by shocks, as has been inferred in other studies of NGC 4151 (e.g., D. R. A. Williams et al. 2020). The B-field is aligned with the jet direction in the ‘sheath’, consistent with shear due to jet–medium interaction. If true, the magnetic field stratification could be consistent with a velocity stratification in the radio outflow of NGC 4151, similar to what is observed in FRI radio galaxies (e.g., 3C 31; R. A. Laing & A. H. Bridle 2002). We get to observe a combined effect of jet ‘spine + sheath’ in the lower resolution 3 GHz image of NGC 4151. Along the eastern receding outflow, a transverse component with B-fields perpendicular to the jet is observed. We identify this to be a ‘wind’ component, threaded by toroidal or helical B-fields similar to that suggested in M. Mehdipour & E. Costantini (2019). The suggestion of a helical field is consistent with the RM gradient that is observed in this feature.

The ‘jet spine’ can be traced up to ~ 3 arcsec (~ 0.03 kpc), while the sheath extends further, up to ~ 4 arcsec (~ 0.04 kpc) from the centre. The persistence of the sheath to larger distances likely arises from jet–medium interaction at the boundaries, which re-energizes particles and produces synchrotron emission. There is a lack of adequate resolution in the spectral index and polarization images from the current data to see these boundary layers and test this hypothesis. High-resolution polarization observations with the e-MERLIN telescope are being planned for this purpose. The absence of a clear ‘wind’ component on the approaching jet side may be attributed to either stronger interactions in inhomogeneous media or the prominence of the jet, which outshines the relatively faint ‘wind’ emission.

4.2. A Magnetically driven outflow in NGC 4151?

We now check whether the outflow in NGC 4151 is magnetically-driven based on the radio and X-ray data. Winds in AGN can be powered by radiation pressure, magnetic pressure, or thermal pressure, as denoted by the equation of motion, $\rho \frac{Dv}{Dt} + \rho \nabla \Phi = -\nabla P + \frac{1}{4\pi} (\nabla \times B) \times B + \rho F^{\text{rad}}$. Terms on the left-hand side represent the force per unit volume to accelerate the fluid, and the gravitational force per unit volume restricting the fluid from flowing out. The terms on the right side represent the force due to gas pressure, the Lorentz force, and the radiation pressure force, respectively (D. M. Crenshaw et al. 2003; D. Proga 2007). For an outflow to originate, any of the forces on the right-hand side must exceed the gravitational force. Radiative winds are typically observed in massive AGN with high optical/UV luminosity, and are less important in the case of low-luminosity AGN (S. Veilleux et al. 2005; D. Proga 2007; M. Farcy et al. 2025) like NGC 4151 (D. R. A. Williams et al. 2020). To understand whether these winds are magnetically or thermally powered, it is necessary to estimate both the magnetic and thermal gas pressure. The magnetic pressure is defined as $B^2/8\pi$ (see M. S. Longair 2011). From the minimum energy condition, the B-field in the ‘wind’ region is found to be $28 - 86 \mu\text{G}$, and at the ‘core’ it is $100 - 300 \mu\text{G}$. Since this provides the B-field strength in one direction, we should multiply this by $\sqrt{3}$ to obtain the total B-field strength, using the condition of isotropy. Hence, the magnetic field pressure in the ‘wind’ region is $(1 - 9) \times 10^{-10} \text{ dyne cm}^{-2}$, and in the ‘core’ is $(12 - 107) \times 10^{-10} \text{ dyne cm}^{-2}$.

The ‘wind’ component observed in NGC 4151 extends out to ~ 400 parsec. This structure exhibits a toroidal B-field with a relatively high degree of polarization (fractional polarization in the ‘wind’ region is found to be $\sim 33\%$ at 10 GHz). This supports the suggestion that the wind could be an AGN accretion disk wind rather than a galactic wind from starburst activity (E. J. M. Colbert et al. 1996b; R. Beck et al. 1996; S. Veilleux et al. 2005), where the fractional polarization is typically $\leq 5\%$, both at lower (e.g., at ~ 1.5 GHz in NGC 1134, NGC 253, UGC 903; B. Sebastian et al. 2020) and at higher frequencies (e.g., at ~ 8 GHz in M 82; H. P. Reuter et al. 1994), due to the lack of large-scale organised B-fields in the outflowing gas. Moreover, we find that the RM values are positive in the northern ‘wind’ component but negative in the southern ‘wind’ component (see Figure 7). Closer to the nucleus, the RM values on the northern and southern sides become comparable, before exhibiting a reversal in sign. This strongly supports the

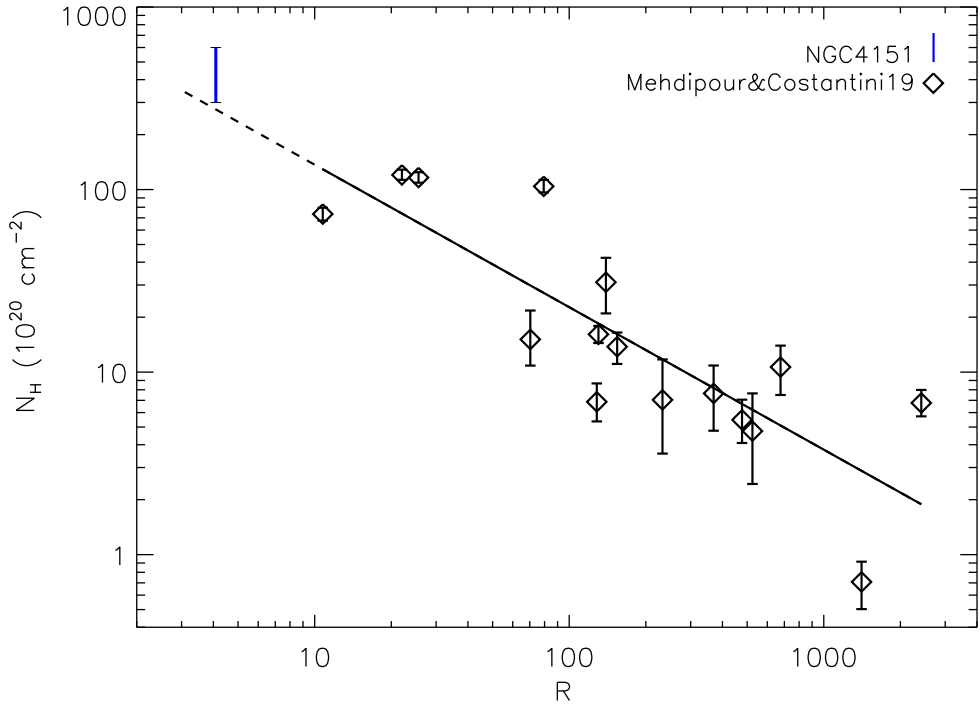


Figure 5. Values of N_{H} and the radio loudness parameter, R , estimated for NGC 4151 (blue bar) superimposed to the anti-correlation (black line) found for radio-loud sources (black diamonds, M. Mehdi & E. Costantini 2019). The dashed line simply extends the correlation to our estimate for NGC 4151.

picture of a helical B-field threading a wide-angle bi-conical ‘wind’ component (also see Figure 1 in S. Ghosh et al. 2025b).

Diffuse soft X-ray gas has been observed in NGC 4151 extending up to ~ 2 kpc, suggested as a thermal plasma with a temperature of about $0.25 - 0.58$ keV. The hot gas pressure is estimated as $\sim 2n_e kT$ and is found as 6.8×10^{-10} dyne cm $^{-2}$ from close to the NLR. It can be as low as 5×10^{-12} dyne cm $^{-2}$ when reaching equilibrium with the neutral hydrogen gas in the galaxy (J. Wang et al. 2010, 2011). Hence, the magnetic pressure exceeds the gas pressure in NGC 4151. The outflow, therefore, appears to be magnetically driven (also see S. B. Kraemer et al. 2020). Magnetocentrifugal winds from the accretion disk usually corotate unless the poloidal magnetic field is extremely powerful. As the rotation in the disk happens differentially, the toroidal component of the magnetic field is easily built (and is much stronger than the poloidal one), the magnetic pressure of which drives these slow-moving outflowing winds (R. D. Blandford & D. G. Payne 1982; Y. Uchida & K. Shibata 1985; R. E. Pudritz & C. A. Norman 1986; R. T. Emmering et al. 1992; J. Contopoulos 1995). These results are also consistent with the suggestion of toroidal or helical B-fields from the RM gradient in NGC 4151. J. F. Gallimore et al. (2024) have been able to find direct evidence for such a hydromagnetic wind in the Seyfert galaxy, NGC 1068, by studying the H_2O megamasers with the High Sensitivity Array (HSA).

4.3. Constraints on the Warm Absorber

The soft X-ray spectrum of NGC 4151 is dominated by emission lines (e.g., N. J. Schurch et al. 2004; S. B. Kraemer et al. 2006), making it less straightforward to identify all the absorption components. However, two absorption components have been consistently reported by the *Chandra* observatory (e.g. J. D. Couto et al. 2016). In particular, one of them has been directly put in relation with the absorption components detected in the UV (S. B. Kraemer et al. 2006), indicating a low-ionization component. In M. Mehdi & E. Costantini (2019), the column density of the low-ionization components of the warm absorber have been put in relation with the radio loudness parameter, R , for a sample of radio-loud AGN, finding a robust anti-correlation between the amount of material available to form a warm absorber in the disk and the radio power. We attempted to locate NGC 4151 ($R \sim 3.09$; L. C. Ho & C. Y. Peng 2001) in this anti-correlation (Figure 5), adopting the column density of the low-ionization component reported in J. D. Couto et al. (2016) as a lower limit for the warm absorber that might have been detected in the RGS band

($N_{\text{H}} \sim 3 - 6 \times 10^{22} \text{ cm}^{-2}$, taking into account the moderate variability of this component). Other, even lower ionization components might still be present. Importantly, Figure 5 shows that the disk-wind connection with the jet emission found for radio-loud sources (M. Mehdipour & E. Costantini 2019) may be extended to radio-quiet objects.

The highly ionized X-ray absorber with a column density of $N_{\text{H}} \sim 3.2 \times 10^{22} \text{ cm}^{-2}$ (D. M. Crenshaw & S. B. Kraemer 2012; J. D. Couto et al. 2016) represents the innermost component of the warm absorber, likely originating from MHD disk winds. The outflow, with a velocity of $v_r \approx -500 \text{ km s}^{-1}$, is located at a radial distance of $r \approx (2.5 - 30) \times 10^{16} \text{ cm}$ from the central engine, corresponding to gas densities of $n_{\text{H}} \sim 10^6 \text{ cm}^{-3}$ (D. M. Crenshaw & S. B. Kraemer 2012; J. D. Couto et al. 2016). Assuming a spherically symmetric outflow (consistent with D. M. Crenshaw et al. 2003; D. M. Crenshaw & S. B. Kraemer 2012), the total gas mass can be expressed as

$$M_{\text{gas}} = 4\pi r^2 C_f \mu m_p N_{\text{H}}, \quad (10)$$

where $\mu = 1.4$ (for solar composition) is the mean atomic weight, m_p is the proton mass, and C_f is the global covering fraction. For $C_f \sim 0.5$, the estimated gas mass lies in the range $M_{\text{gas}} \sim (0.15 - 21) M_{\odot}$. The corresponding mass outflow rate,

$$\dot{M}_{\text{gas}} = 4\pi r C_f \mu m_p N_{\text{H}} v_r, \quad (11)$$

is $\dot{M}_{\text{gas}} \approx 0.01 - 0.1 M_{\odot} \text{ yr}^{-1}$, implying a kinetic luminosity

$$L_{\text{KE}} = \frac{1}{2} \dot{M}_{\text{gas}} v_r^2 = 2\pi r C_f \mu m_p N_{\text{H}} v_r^3, \quad (12)$$

of $L_{\text{KE}} \approx (0.7 - 8.2) \times 10^{39} \text{ erg s}^{-1}$.

Although the mass outflow rate is comparable to or exceeds the inferred accretion rate by a factor of 1 – 10, the mechanical power constitutes less than 0.01% of the bolometric luminosity, as was also found for the radio ‘wind’ component (see Section 3.3). The force multiplier (= ratio of the total photo-absorption cross-section to the Thomson cross-section) for this source, obtained by CLOUDY modeling, is found to be near unity, making radiative driving inefficient in sub-Eddington AGN, and hence implying that mechanisms such as MHD-driven outflow must be responsible for their acceleration (D. M. Crenshaw & S. B. Kraemer 2012; S. B. Kraemer et al. 2018). This indicates that, while the outflow is mass-loaded, its kinetic coupling efficiency is low, consistent with a slow, magnetically driven wind rather than a radiatively accelerated one. The relatively small gas mass (M_{gas}) compared to that required for the mixed thermal plasma inferred from internal depolarization modeling (see Section 3.2.1) further suggests that at least one external Faraday-rotating screen contributes to the observed depolarization. Thus, the physical conditions point toward a magnetically dominated, low-efficiency outflow in the nuclear region, characteristic of radio-quiet Seyfert nuclei.

5. CONCLUSIONS

We have observed the Seyfert galaxy NGC 4151 with the VLA B-array configuration at 3 and 10 GHz and detected a stratified outflow based on the inferred magnetic field structures. We summarize the primary findings of our study below.

1. The 3 GHz VLA image of NGC 4151 reveals the well-known east–west radio outflow, with a hotspot-like region in the eastern lobe. Additional diffuse emission is detected perpendicular to the east–west outflow. The inferred B-fields, after source RM correction, remain aligned with the outflow at the jet edge and perpendicular towards the inner region. Besides, the B-fields are found perpendicular to the transverse outflow component surrounding the jet. These structures and inferred B-fields are consistent with the jet+wind model of M. Mehdipour & E. Costantini (2019).
2. The 10 GHz VLA image resolves the outflow into a jet ‘spine’ with perpendicular B-fields and a jet ‘sheath’ with aligned B-fields. The hotspot-like region is clearly seen with B-fields resembling oblique shocks. The base of the wind-like feature seen in the 3 GHz image is also visible at 10 GHz. The perpendicular B-fields in the jet ‘spine’ are consistent with shocks as have been suggested in the case of NGC 4151 from various studies in the literature (J. Wang et al. 2010; D. R. A. Williams et al. 2020). The aligned B-fields in the ‘sheath’ are consistent with shearing due to jet-medium interaction.

3. The jet velocity ~ 0.1 kpc away from the nucleus is estimated to be $\sim 0.16c$ from the jet-to-counterjet intensity ratio assuming Doppler boosting effects and a jet inclination of 40 degrees. The jet kinetic power, derived from the core radio luminosity, is $\sim 10^{43}$ erg s $^{-1}$, which is at the higher end of jet powers typically observed in radio-quiet AGN.
4. We derive an electron density of $0.004 - 0.02$ cm $^{-3}$ and a characteristic extent of $0.06 - 0.2$ kpc for the Faraday rotating medium around the jet in NGC 4151. These estimates are consistent with either a sparse warm ionized medium in the host galaxy or a magnetized sheath or cocoon surrounding the jet and acting as the Faraday screen. Assuming internal depolarization in the wider ‘wind’ outflow of NGC 4151 as thermal gas is mixed with synchrotron-emitting plasma (consistent with strong depolarization in the ‘wind’ region), we estimate the thermal gas mass to be $\sim 10^3 M_\odot$. From the warm absorber mass estimates in NGC 4151, it is evident that the mixing of this gas cannot be solely responsible for the observed depolarization. It is essential to have an additional external screen to fully explain the observed depolarization.
5. The identified radio ‘wind’ component is found to be heavy with a mass of $1050 - 3200 M_\odot$, with an outflow rate ($= 0.01 - 0.03 M_\odot$ yr $^{-1}$) higher than the black hole accretion rate, although the kinetic power ($\sim 0.01 - 0.5\%$ of L_{bol}) is small, suggesting the presence of massive but kinematically weak winds, ineffective in providing galactic-scale feedback. We also observe a transverse RM gradient ranging from $+75$ to -25 rad m $^{-2}$ across the (northern side of) ‘wind’ component, suggestive of a helical magnetic field threading it. Although limited spatial resolution implies that systematic effects exist, similar RM values with opposite signs in the northern and southern ‘wind’ components point to an underlying coherent magnetic field structure. Taken together these components support the presence of a large-scale transverse RM gradient and thereby the presence of a helical magnetic field across the wide-angled bi-conical wind.
6. The ‘minimum energy’ B-field strength ranges from $100 - 300$ μ G in the ‘core’ region to $28 - 86$ μ G in the ‘wind’ region, ~ 0.5 kpc from the core. The corresponding magnetic pressure decreases from $(12 - 107) \times 10^{-10}$ dyne cm $^{-2}$ in the core to $(1 - 9) \times 10^{-10}$ dyne cm $^{-2}$ in the ‘wind’. On the other hand, the thermal gas pressure decreases from 6.8×10^{-10} dyne cm $^{-2}$ from close to the NLR to 5×10^{-12} dyne cm $^{-2}$ in the galactic outskirts. Across different spatial scales, the magnetic pressure exceeds the thermal gas pressure, indicating that the outflow in NGC 4151 is magnetically-driven. The presence of MHD winds in this source has been previously discussed by [D. M. Crenshaw & S. B. Kraemer \(2012\)](#); [S. B. Kraemer et al. \(2018\)](#).
7. We find that the amount of material available to launch an UV/X-ray wind, given the radio-to-optical flux density ratio (R) for this source, follows the same trend as found for radio-loud objects. This suggests that a disk-wind radio connection might also be at play for relatively radio-weak sources. Moreover, the kinetic power of the high-ionization gas present at $(2.5 - 30) \times 10^{16}$ cm is found to be low i.e., $L_{\text{KE}} \approx (0.7 - 8.2) \times 10^{39}$ erg s $^{-1} < 0.01\% L_{\text{bol}}$, but similar to the radio-detected ‘wind’ in NGC 4151.

6. ACKNOWLEDGEMENT

We thank the referee for their suggestions which have significantly improved our manuscript. SG and PK acknowledge the support of the Department of Atomic Energy, Government of India, under the project 12-R&D-TFR-5.02-0700. This research has utilised data from the National Radio Astronomy Observatory (NRAO) facility. The NRAO and Green Bank Observatory are facilities of the U.S. National Science Foundation operated under cooperative agreement by Associated Universities, Inc.

7. APPENDIX

Figure 6 presents the polarized intensity images at 3 and 10 GHz in the left and right panels, respectively. In both bands, the core exhibits the highest polarized intensity, which progressively decreases with distance from the core. The jet axis or the ‘spine’ shows systematically higher polarized intensity than the surrounding ‘sheath’, whereas the ‘sheath’ displays a higher fractional polarization as in Figure 1. We also present the transverse slices from the RM image showing gradients in the ‘wind’ region in Figure 7. These are consistent with the presence of 100-parsec-scale helical magnetic fields threading the ‘wind’ component.

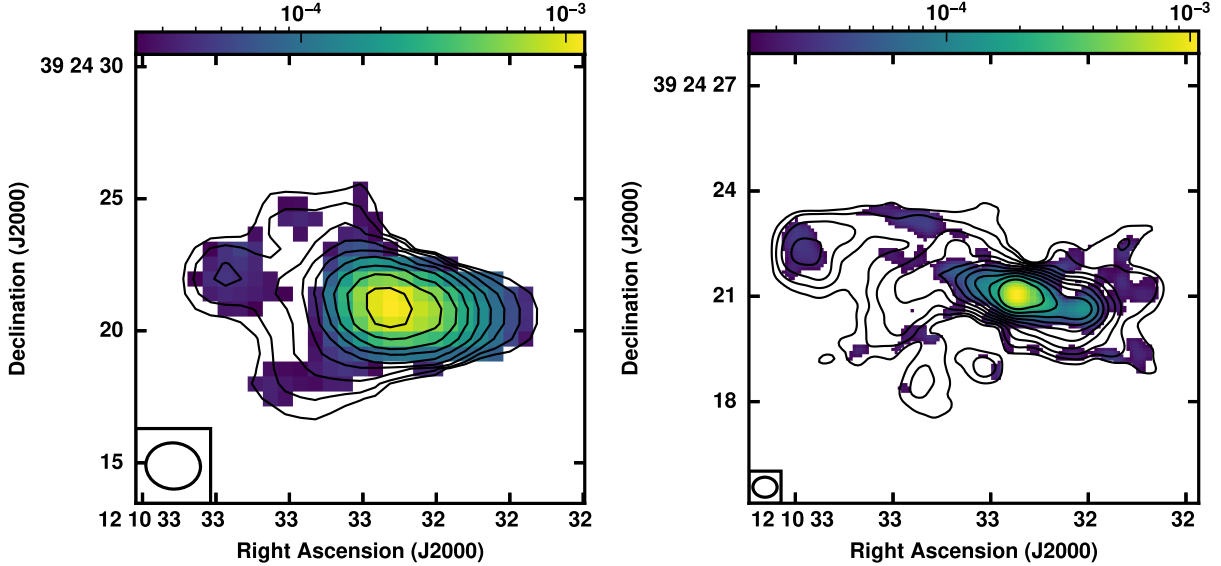


Figure 6. Left: 3 GHz polarisation intensity in colour in logarithmic scale, ranging from $24 \mu\text{Jy beam}^{-1}$ to $1.2 \text{ mJy beam}^{-1}$. The total intensity contours at 3 GHz are shown in black as above. Right: 10 GHz polarization intensity in colour in logarithmic scale, ranging from $15 \mu\text{Jy beam}^{-1}$ to $1.1 \text{ mJy beam}^{-1}$. The total intensity contours at 10 GHz are shown in black as above.

AUTHOR CONTRIBUTIONS

The author order is consistent with their contributions to this work.

Facilities: VLA

Software: CASA (J. P. McMullin et al. 2007)

REFERENCES

Asada, K., Inoue, M., Uchida, Y., et al. 2002, PASJ, 54, L39, doi: [10.1093/pasj/54.3.L39](https://doi.org/10.1093/pasj/54.3.L39)

Baum, S. A., O'Dea, C. P., Dallacassa, D., de Bruyn, A. G., & Pedlar, A. 1993, ApJ, 419, 553, doi: [10.1086/173508](https://doi.org/10.1086/173508)

Beck, R., Brandenburg, A., Moss, D., Shukurov, A., & Sokoloff, D. 1996, ARA&A, 34, 155, doi: [10.1146/annurev.astro.34.1.155](https://doi.org/10.1146/annurev.astro.34.1.155)

Beck, R., & Wielebinski, R. 2013, in Planets, Stars and Stellar Systems. Volume 5: Galactic Structure and Stellar Populations, ed. T. D. Oswalt & G. Gilmore, Vol. 5, 641, doi: [10.1007/978-94-007-5612-0_13](https://doi.org/10.1007/978-94-007-5612-0_13)

Begelman, M. C., & Cioffi, D. F. 1989, ApJL, 345, L21, doi: [10.1086/185542](https://doi.org/10.1086/185542)

Bentz, M. C., Williams, P. R., & Treu, T. 2022, ApJ, 934, 168, doi: [10.3847/1538-4357/ac7c0a](https://doi.org/10.3847/1538-4357/ac7c0a)

Bhatnagar, S., Rau, U., & Golap, K. 2013, ApJ, 770, 91, doi: [10.1088/0004-637X/770/2/91](https://doi.org/10.1088/0004-637X/770/2/91)

Blandford, R. D., & Payne, D. G. 1982, MNRAS, 199, 883, doi: [10.1093/mnras/199.4.883](https://doi.org/10.1093/mnras/199.4.883)

Blundell, K. M., & Bowler, M. G. 2005, ApJL, 622, L129, doi: [10.1086/429663](https://doi.org/10.1086/429663)

Blustin, A. J., & Fabian, A. C. 2009, MNRAS, 396, 1732, doi: [10.1111/j.1365-2966.2009.14856.x](https://doi.org/10.1111/j.1365-2966.2009.14856.x)

Booler, R. V., Pedlar, A., & Davies, R. D. 1982, MNRAS, 199, 229, doi: [10.1093/mnras/199.2.229](https://doi.org/10.1093/mnras/199.2.229)

Burn, B. J. 1966, MNRAS, 133, 67, doi: [10.1093/mnras/133.1.67](https://doi.org/10.1093/mnras/133.1.67)

Carral, P., Turner, J. L., & Ho, P. T. P. 1990, ApJ, 362, 434, doi: [10.1086/169280](https://doi.org/10.1086/169280)

Cecil, G., Bland-Hawthorn, J., Veilleux, S., & Filippenko, A. V. 2001, ApJ, 555, 338, doi: [10.1086/321481](https://doi.org/10.1086/321481)

Cioffi, D. F., & Blondin, J. M. 1992, ApJ, 392, 458, doi: [10.1086/171445](https://doi.org/10.1086/171445)

Colbert, E. J. M., Baum, S. A., Gallimore, J. F., O'Dea, C. P., & Christensen, J. A. 1996a, ApJ, 467, 551, doi: [10.1086/177633](https://doi.org/10.1086/177633)

Colbert, E. J. M., Baum, S. A., Gallimore, J. F., et al. 1996b, ApJS, 105, 75, doi: [10.1086/192307](https://doi.org/10.1086/192307)

Contopoulos, J. 1995, ApJ, 450, 616, doi: [10.1086/176170](https://doi.org/10.1086/176170)

Cordes, J. M., & Lazio, T. J. W. 2002, arXiv e-prints, astro, doi: [10.48550/arXiv.astro-ph/0207156](https://doi.org/10.48550/arXiv.astro-ph/0207156)

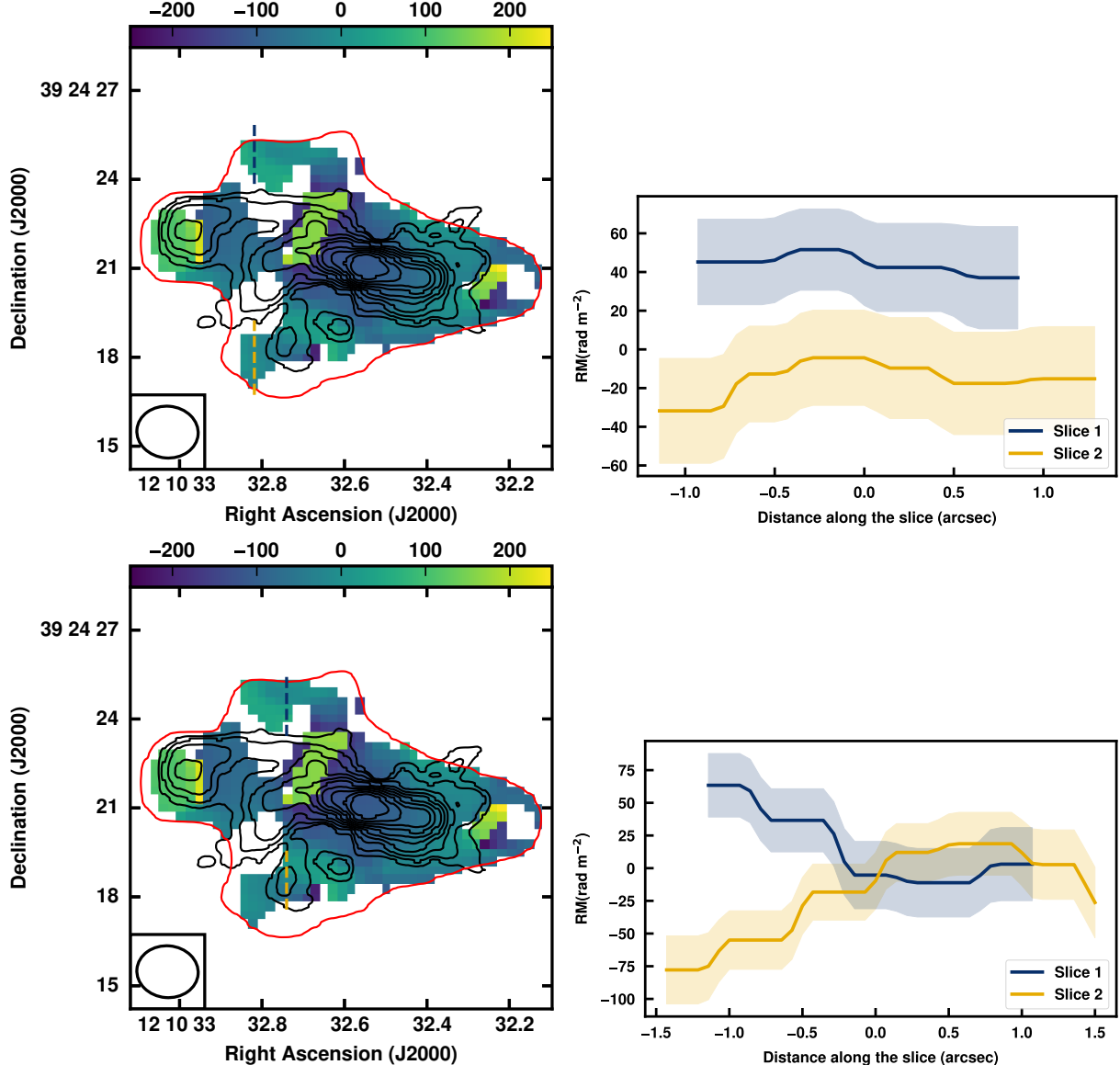


Figure 7. Left panel: RM images showing RM slices taken across the different parts of the ‘wind’ region. The northern and southern ‘wind’ have been indicated with blue and yellow dashed lines, respectively. Right panel: The slices (considered from top to bottom) are shown as a function of distance along with the errors. The northern and southern ‘wind’ show similar absolute value of RM but with a changed direction, indicating a reversal of the B-field direction along our line of sight between the two sides. Such an RM gradient may indicate the presence of helical fields along a conical envelope of synchrotron winds.

Couto, J. D., Kraemer, S. B., Turner, T. J., & Crenshaw, D. M. 2016, ApJ, 833, 191, doi: [10.3847/1538-4357/833/2/191](https://doi.org/10.3847/1538-4357/833/2/191)

Crenshaw, D. M., & Kraemer, S. B. 2007, ApJ, 659, 250, doi: [10.1086/511970](https://doi.org/10.1086/511970)

Crenshaw, D. M., & Kraemer, S. B. 2012, ApJ, 753, 75, doi: [10.1088/0004-637X/753/1/75](https://doi.org/10.1088/0004-637X/753/1/75)

Crenshaw, D. M., Kraemer, S. B., & George, I. M. 2003, ARA&A, 41, 117, doi: [10.1146/annurev.astro.41.082801.100328](https://doi.org/10.1146/annurev.astro.41.082801.100328)

Emmering, R. T., Blandford, R. D., & Shlosman, I. 1992, ApJ, 385, 460, doi: [10.1086/170955](https://doi.org/10.1086/170955)

Farcy, M., Hirschmann, M., Somerville, R. S., et al. 2025, MNRAS, 543, 967, doi: [10.1093/mnras/staf1464](https://doi.org/10.1093/mnras/staf1464)

Faucher-Giguère, C.-A., & Quataert, E. 2012, MNRAS, 425, 605, doi: [10.1111/j.1365-2966.2012.21512.x](https://doi.org/10.1111/j.1365-2966.2012.21512.x)

Feain, I. J., Ekers, R. D., Murphy, T., et al. 2009, ApJ, 707, 114, doi: [10.1088/0004-637X/707/1/114](https://doi.org/10.1088/0004-637X/707/1/114)

Fendt, C. 2006, ApJ, 651, 272, doi: [10.1086/507976](https://doi.org/10.1086/507976)

Feng, H.-C., Li, S.-S., Bai, J. M., et al. 2024, ApJ, 976, 176, doi: [10.3847/1538-4357/ad8568](https://doi.org/10.3847/1538-4357/ad8568)

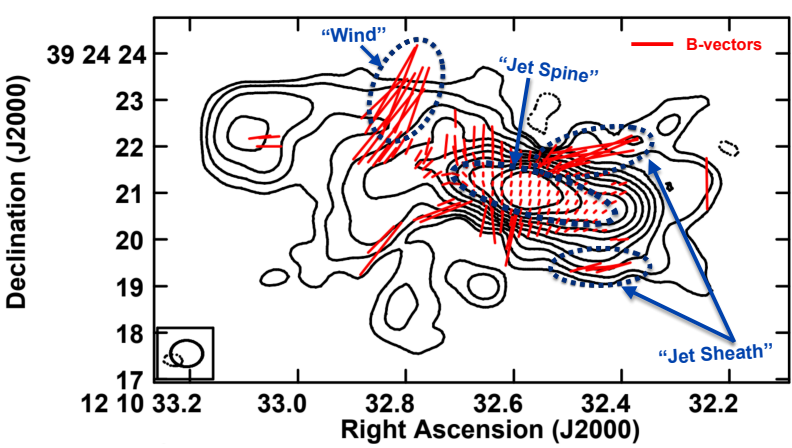
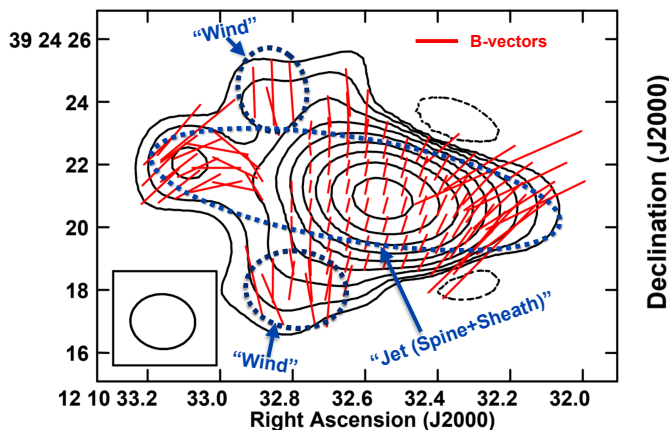


Figure 8. 3 GHz (left) and 10 GHz (right) image showing B-field vectors corrected for Galactic plus source RM. The contours and the polarization vector lengths are the same as Figure 1.

Fiore, F., Feruglio, C., Shankar, F., et al. 2017, A&A, 601, A143, doi: [10.1051/0004-6361/201629478](https://doi.org/10.1051/0004-6361/201629478)

Gabuzda, D. C., Murray, É., & Cronin, P. 2004, MNRAS, 351, L89, doi: [10.1111/j.1365-2966.2004.08037.x](https://doi.org/10.1111/j.1365-2966.2004.08037.x)

Gaensler, B. M., Madsen, G. J., Chatterjee, S., & Mao, S. A. 2008, PASA, 25, 184, doi: [10.1071/AS08004](https://doi.org/10.1071/AS08004)

Gallimore, J. F., Impellizzeri, C. M. V., Aghelpasand, S., et al. 2024, ApJL, 975, L9, doi: [10.3847/2041-8213/ad864f](https://doi.org/10.3847/2041-8213/ad864f)

Garrington, S. T., Leahy, J. P., Conway, R. G., & Laing, R. A. 1988, Nature, 331, 147, doi: [10.1038/331147a0](https://doi.org/10.1038/331147a0)

Ghosh, S., Kharb, P., Sajjanhar, E., Pasetto, A., & Sebastian, B. 2025a, ApJ, 989, 40, doi: [10.3847/1538-4357/ade98d](https://doi.org/10.3847/1538-4357/ade98d)

Ghosh, S., Kharb, P., Sebastian, B., et al. 2025b, arXiv e-prints, arXiv:2509.15355, doi: [10.48550/arXiv.2509.15355](https://doi.org/10.48550/arXiv.2509.15355)

Gianolli, V. E., Kim, D. E., Bianchi, S., et al. 2023, MNRAS, 523, 4468, doi: [10.1093/mnras/stad1697](https://doi.org/10.1093/mnras/stad1697)

Giroletti, M., & Panessa, F. 2009, ApJL, 706, L260, doi: [10.1088/0004-637X/706/2/L260](https://doi.org/10.1088/0004-637X/706/2/L260)

Hjellming, R. M., & Johnston, K. J. 1981, ApJL, 246, L141, doi: [10.1086/183571](https://doi.org/10.1086/183571)

Ho, L. C., & Peng, C. Y. 2001, ApJ, 555, 650, doi: [10.1086/321524](https://doi.org/10.1086/321524)

Hopkins, P. F., & Elvis, M. 2010, MNRAS, 401, 7, doi: [10.1111/j.1365-2966.2009.15643.x](https://doi.org/10.1111/j.1365-2966.2009.15643.x)

Hovatta, T., Lister, M. L., Aller, M. F., et al. 2012, AJ, 144, 105, doi: [10.1088/0004-6256/144/4/105](https://doi.org/10.1088/0004-6256/144/4/105)

Ishibashi, W., & Courvoisier, T. J. L. 2011, A&A, 525, A118, doi: [10.1051/0004-6361/201014987](https://doi.org/10.1051/0004-6361/201014987)

Johnston, K. J., Elvis, M., Kjer, D., & Shen, B. S. P. 1982, ApJ, 262, 61, doi: [10.1086/160396](https://doi.org/10.1086/160396)

Kellermann, K. I., Sramek, R., Schmidt, M., Shaffer, D. B., & Green, R. 1989, AJ, 98, 1195, doi: [10.1086/115207](https://doi.org/10.1086/115207)

Kharb, P., Gabuzda, D. C., O'Dea, C. P., Shastri, P., &

Baum, S. A. 2009, ApJ, 694, 1485, doi: [10.1088/0004-637X/694/2/1485](https://doi.org/10.1088/0004-637X/694/2/1485)

Kharb, P., Subramanian, S., Das, M., Vaddi, S., & Paragi, Z. 2021, ApJ, 919, 108, doi: [10.3847/1538-4357/ac0c82](https://doi.org/10.3847/1538-4357/ac0c82)

Kochanek, C. S., & Hawley, J. F. 1990, ApJ, 350, 561, doi: [10.1086/168411](https://doi.org/10.1086/168411)

Kraemer, S. B., Tombesi, F., & Bottorff, M. C. 2018, ApJ, 852, 35, doi: [10.3847/1538-4357/aa9ce0](https://doi.org/10.3847/1538-4357/aa9ce0)

Kraemer, S. B., Turner, T. J., Couto, J. D., et al. 2020, MNRAS, 493, 3893, doi: [10.1093/mnras/staa428](https://doi.org/10.1093/mnras/staa428)

Kraemer, S. B., Turner, T. J., Crenshaw, D. M., et al. 2021, in IAU Symposium, Vol. 359, Galaxy Evolution and Feedback across Different Environments, ed. T. Storchi Bergmann, W. Forman, R. Overzier, & R. Riffel, 131–135, doi: [10.1017/S1743921320001660](https://doi.org/10.1017/S1743921320001660)

Kraemer, S. B., Crenshaw, D. M., Gabel, J. R., et al. 2006, ApJS, 167, 161, doi: [10.1086/508629](https://doi.org/10.1086/508629)

La Rosa, T. N., Shore, S. N., Joseph, T., Lazio, W., & Kassim, N. E. 2006, in Journal of Physics Conference Series, Vol. 54, Journal of Physics Conference Series, ed.

R. Schödel, G. C. Bower, M. P. Muno, S. Nayakshin, & T. Ott (IOP), 10–15, doi: [10.1088/1742-6596/54/1/002](https://doi.org/10.1088/1742-6596/54/1/002)

Laing, R. A. 1980, MNRAS, 193, 439, doi: [10.1093/mnras/193.3.439](https://doi.org/10.1093/mnras/193.3.439)

Laing, R. A. 1988, Nature, 331, 149, doi: [10.1038/331149a0](https://doi.org/10.1038/331149a0)

Laing, R. A., & Bridle, A. H. 2002, MNRAS, 336, 328, doi: [10.1046/j.1365-8711.2002.05756.x](https://doi.org/10.1046/j.1365-8711.2002.05756.x)

Laing, R. A., & Bridle, A. H. 2014, MNRAS, 437, 3405, doi: [10.1093/mnras/stt2138](https://doi.org/10.1093/mnras/stt2138)

Laing, R. A., Bridle, A. H., Parma, P., & Murgia, M. 2008, MNRAS, 391, 521, doi: [10.1111/j.1365-2966.2008.13895.x](https://doi.org/10.1111/j.1365-2966.2008.13895.x)

Laing, R. A., Canvin, J. R., Cotton, W. D., & Bridle, A. H. 2006, MNRAS, 368, 48, doi: [10.1111/j.1365-2966.2006.10099.x](https://doi.org/10.1111/j.1365-2966.2006.10099.x)

Lisakov, M. M., Kravchenko, E. V., Pushkarev, A. B., et al. 2021, *ApJ*, 910, 35, doi: [10.3847/1538-4357/abe1bd](https://doi.org/10.3847/1538-4357/abe1bd)

Longair, M. S. 2011, *High Energy Astrophysics*

May, D., & Steiner, J. E. 2017, *MNRAS*, 469, 994, doi: [10.1093/mnras/stx886](https://doi.org/10.1093/mnras/stx886)

McMullin, J. P., Waters, B., Schiebel, D., Young, W., & Golap, K. 2007, in *Astronomical Society of the Pacific Conference Series*, Vol. 376, *Astronomical Data Analysis Software and Systems XVI*, ed. R. A. Shaw, F. Hill, & D. J. Bell, 127

Mehdipour, M., & Costantini, E. 2019, *A&A*, 625, A25, doi: [10.1051/0004-6361/201935205](https://doi.org/10.1051/0004-6361/201935205)

Merloni, A., & Heinz, S. 2007, *MNRAS*, 381, 589, doi: [10.1111/j.1365-2966.2007.12253.x](https://doi.org/10.1111/j.1365-2966.2007.12253.x)

Mundell, C. G., Pedlar, A., Baum, S. A., et al. 1995, *MNRAS*, 272, 355, doi: [10.1093/mnras/272.2.355](https://doi.org/10.1093/mnras/272.2.355)

Mundell, C. G., Pedlar, A., Shone, D. L., & Robinson, A. 1999, *MNRAS*, 304, 481, doi: [10.1046/j.1365-8711.1999.02331.x](https://doi.org/10.1046/j.1365-8711.1999.02331.x)

Mundell, C. G., Wrobel, J. M., Pedlar, A., & Gallimore, J. F. 2001, in *IAU Symposium*, Vol. 205, *Galaxies and their Constituents at the Highest Angular Resolutions*, ed. R. T. Schilizzi, 192, doi: [10.48550/arXiv.astro-ph/0012229](https://doi.org/10.48550/arXiv.astro-ph/0012229)

Mundell, C. G., Wrobel, J. M., Pedlar, A., & Gallimore, J. F. 2003, *ApJ*, 583, 192, doi: [10.1086/345356](https://doi.org/10.1086/345356)

O'Dea, C. P., & Owen, F. N. 1987, *ApJ*, 316, 95, doi: [10.1086/165182](https://doi.org/10.1086/165182)

O'Sullivan, S. P., & Gabuzda, D. C. 2009, *MNRAS*, 393, 429, doi: [10.1111/j.1365-2966.2008.14213.x](https://doi.org/10.1111/j.1365-2966.2008.14213.x)

O'Sullivan, S. P., Feain, I. J., McClure-Griffiths, N. M., et al. 2013, *ApJ*, 764, 162, doi: [10.1088/0004-637X/764/2/162](https://doi.org/10.1088/0004-637X/764/2/162)

Pacholczyk, A. G. 1970, *Radio astrophysics. Nonthermal processes in galactic and extragalactic sources*

Pacholczyk, A. G., & Scott, J. S. 1976, *ApJ*, 203, 313

Panessa, F., Baldi, R. D., Laor, A., et al. 2019, *Nature Astronomy*, 3, 387, doi: [10.1038/s41550-019-0765-4](https://doi.org/10.1038/s41550-019-0765-4)

Pasetto, A., Carrasco-González, C., Gómez, J. L., et al. 2021, *ApJL*, 923, L5, doi: [10.3847/2041-8213/ac3a88](https://doi.org/10.3847/2041-8213/ac3a88)

Pedlar, A., Howley, P., Axon, D. J., & Unger, S. W. 1992, *MNRAS*, 259, 369, doi: [10.1093/mnras/259.2.369](https://doi.org/10.1093/mnras/259.2.369)

Peretti, E., Peron, G., Tombesi, F., et al. 2025, *JCAP*, 2025, 013, doi: [10.1088/1475-7516/2025/07/013](https://doi.org/10.1088/1475-7516/2025/07/013)

Perucho, M., Bosch-Ramon, V., & Barkov, M. V. 2017, *A&A*, 606, A40, doi: [10.1051/0004-6361/201630117](https://doi.org/10.1051/0004-6361/201630117)

Proga, D. 2007, in *Astronomical Society of the Pacific Conference Series*, Vol. 373, *The Central Engine of Active Galactic Nuclei*, ed. L. C. Ho & J. W. Wang, 267, doi: [10.48550/arXiv.astro-ph/0701100](https://doi.org/10.48550/arXiv.astro-ph/0701100)

Pudritz, R. E., & Norman, C. A. 1986, *ApJ*, 301, 571, doi: [10.1086/163924](https://doi.org/10.1086/163924)

Pudritz, R. E., Rogers, C. S., & Ouyed, R. 2006, *MNRAS*, 365, 1131, doi: [10.1111/j.1365-2966.2005.09766.x](https://doi.org/10.1111/j.1365-2966.2005.09766.x)

Radcliffe, J. F., Barthel, P. D., Garrett, M. A., et al. 2021, *A&A*, 649, L9, doi: [10.1051/0004-6361/202140791](https://doi.org/10.1051/0004-6361/202140791)

Reuter, H. P., Klein, U., Lesch, H., Wielebinski, R., & Kronberg, P. P. 1994, *A&A*, 282, 724

Romanova, M. M., Ustyugova, G. V., Koldoba, A. V., & Lovelace, R. V. E. 2009, *MNRAS*, 399, 1802, doi: [10.1111/j.1365-2966.2009.15413.x](https://doi.org/10.1111/j.1365-2966.2009.15413.x)

Ruiz, M., Young, S., Packham, C., Alexander, D. M., & Hough, J. H. 2003, *MNRAS*, 340, 733, doi: [10.1046/j.1365-8711.2003.06239.x](https://doi.org/10.1046/j.1365-8711.2003.06239.x)

Schurch, N. J., Warwick, R. S., Griffiths, R. E., & Kahn, S. M. 2004, *MNRAS*, 350, 1, doi: [10.1111/j.1365-2966.2004.07632.x](https://doi.org/10.1111/j.1365-2966.2004.07632.x)

Sebastian, B., Kharb, P., O'Dea, C. P., Gallimore, J. F., & Baum, S. A. 2020, *MNRAS*, 499, 334, doi: [10.1093/mnras/staa2473](https://doi.org/10.1093/mnras/staa2473)

Shapovalova, A. I., Popović, L. Č., Burenkov, A. N., et al. 2010, *A&A*, 509, A106, doi: [10.1051/0004-6361/200912311](https://doi.org/10.1051/0004-6361/200912311)

Silpa, S., Kharb, P., O'Dea, C. P., et al. 2021, *MNRAS*, 507, 2550, doi: [10.1093/mnras/stab2110](https://doi.org/10.1093/mnras/stab2110)

Strickland, D. K., & Stevens, I. R. 2000, *MNRAS*, 314, 511, doi: [10.1046/j.1365-8711.2000.03391.x](https://doi.org/10.1046/j.1365-8711.2000.03391.x)

THE CASA TEAM, Bean, B., Bhatnagar, S., et al. 2022, *arXiv e-prints*, arXiv:2210.02276, <https://arxiv.org/abs/2210.02276>

Tombesi, F., Cappi, M., Reeves, J. N., et al. 2011, *ApJ*, 742, 44, doi: [10.1088/0004-637X/742/1/44](https://doi.org/10.1088/0004-637X/742/1/44)

Uchida, Y., & Shibata, K. 1985, *PASJ*, 37, 515

Ulvestad, J. S., Roy, A. L., Colbert, E. J. M., & Wilson, A. S. 1998, *ApJ*, 496, 196, doi: [10.1086/305382](https://doi.org/10.1086/305382)

Ulvestad, J. S., Wong, D. S., Taylor, G. B., Gallimore, J. F., & Mundell, C. G. 2005, *AJ*, 130, 936, doi: [10.1086/432034](https://doi.org/10.1086/432034)

Urry, C. M., & Padovani, P. 1995, *PASP*, 107, 803

van Breugel, W., & Fomalont, E. B. 1984, *ApJL*, 282, L55, doi: [10.1086/184304](https://doi.org/10.1086/184304)

van der Laan, H., & Perola, G. C. 1969, *A&A*, 3, 468

Veilleux, S., Cecil, G., & Bland-Hawthorn, J. 2005, *ARA&A*, 43, 769, doi: [10.1146/annurev.astro.43.072103.150610](https://doi.org/10.1146/annurev.astro.43.072103.150610)

Vleugels, C., McClure, M., Sturm, A., & Vlasblom, M. 2025, *A&A*, 695, A145, doi: [10.1051/0004-6361/202452475](https://doi.org/10.1051/0004-6361/202452475)

Wang, J., Fabbiano, G., Elvis, M., et al. 2011, *ApJ*, 736, 62, doi: [10.1088/0004-637X/736/1/62](https://doi.org/10.1088/0004-637X/736/1/62)

Wang, J., Fabbiano, G., Risaliti, G., et al. 2010, ApJL, 719, L208, doi: [10.1088/2041-8205/719/2/L208](https://doi.org/10.1088/2041-8205/719/2/L208)

Williams, D. R. A., McHardy, I. M., Baldi, R. D., et al. 2017, MNRAS, 472, 3842, doi: [10.1093/mnras/stx2205](https://doi.org/10.1093/mnras/stx2205)

Williams, D. R. A., Baldi, R. D., McHardy, I. M., et al. 2020, MNRAS, 495, 3079, doi: [10.1093/mnras/staa1152](https://doi.org/10.1093/mnras/staa1152)

Xiang, X., Miller, J. M., Behar, E., et al. 2025, ApJL, 988, L54, doi: [10.3847/2041-8213/adee9b](https://doi.org/10.3847/2041-8213/adee9b)

Xu, J., & Han, J.-L. 2014, Research in Astronomy and Astrophysics, 14, 942, doi: [10.1088/1674-4527/14/8/005](https://doi.org/10.1088/1674-4527/14/8/005)

Yongkang, Y., Peng, Z., Zhou, L., et al. 2025, PhRvD, 111, 043027, doi: [10.1103/PhysRevD.111.043027](https://doi.org/10.1103/PhysRevD.111.043027)

Zakamska, N. L., & Greene, J. E. 2014, MNRAS, 442, 784, doi: [10.1093/mnras/stu842](https://doi.org/10.1093/mnras/stu842)